Modeling, Fabrication, and Characterization of Optically-Resonant Periodic Electrode Structures

by

Robert Philip Fabrizzio II

Submitted in Partial Fulfillment

of the

Requirements for the Degree

Master of Science

Supervised by

Professor Thomas G. Brown

The Institute of Optics
The College
School of Engineering and Applied Sciences

University of Rochester
Rochester, New York

1998

Curriculum Vitae

The author was born in Norwalk, Connecticut on October 26, 1966. He attended The United States Military Academy from 1984 to 1988, and graduated with a Bachelor of Science degree in Engineering Physics in 1988. Upon graduation, he was commissioned an officer in the United States Army where he has served for over ten years. Sponsored by the Army, he came to the University of Rochester in the Fall of 1996 and began graduate studies in Optics. He pursued his research in integrated optoelectronics under the direction of Professor Thomas G. Brown.

Acknowledgments

I would like to acknowledge the following people who had a direct bearing on the completion of this thesis.

First and foremost, I would like to thank Professor Thomas Brown, who not only provided tremendous guidance and encouragement, but was more than willing to take a lonely Masters' student under his wing. I could not have asked for more from him, as an advisor or a friend.

Dr. Scott Norton and Professor Mike Morris, for allowing me access to the analytical tools necessary to conduct the modeling and optimization that made up such a large part of this work. Craig Olson and Dr. Brian Kruschwitz, for giving me the know-how around the laboratories to successfully fabricate the structures. Brian McIntyre, for both his tireless efforts in examining my seemingly never-ending flow of samples as well as becoming a friend and confidant. I will surely miss our many conversations.

Al Heaney, Dr. Amy Bieber, and Professor Turan Erdogan, for their efforts in enabling the experimental characterization of fabricated samples. Kartik Srinivas, for his assistance in and around the lab. And certainly, Sharon Weiss, for her tremendous experimental work, without which, this paper would have a very short "Results" chapter.

The United States Army and the Department of Physics at the United States Military Academy (particularly COL Raymond Winkel), for funding and sponsoring my Advanced Civil Schooling.

Finally, this paper, like most things in my life, would be empty if not for the love of my life, Stacy, who always reminds me of what is truly important.

Abstract

This thesis presents an effort to model, fabricate, and characterize optically-resonant periodic electrode (ORPEL) structures. The interconnect between electronic components is a major problem that is hindering further improvements in modern communication systems. The realization of low-cost wavelength-selective detectors and wavelength-selective optical switches/modulators would be a major step toward a solution to this problem. Clearly, any "all-optical" technology will likely need some form of electronic control mechanism. An ORPEL structure is an interdigitated array of metal fingers, with its period chosen to satisfy specific resonances. The use of silicon on insulator (SOI) waveguides with an ORPEL overlay was studied as a "building block" structure for resonant interactions in the λ = 820 nm, λ = 1064 nm, and λ = 1550 nm wavelength ranges. These structures can play the role of detectors, optoelectronic modulators, or optical switches.

Structures were initially modeled by first-order methods to provide a maximum off-resonance reflectance. Initial designs were analyzed by rigorous coupled-wave methods, while structure parameters were varied in order to minimize a pre-determined merit function. While undergoing optimization, the grating period of the structure was adjusted in order to return the resonance wavelength back to design.

Experimental results for both λ = 1064 nm and λ = 1550 nm structures verified that modeling and optimization closely matched experiment for the highest quality material. We have concluded that, given a quality waveguide to build upon, it is possible to design and construct an optically-resonant structure that satisfies a particular target wavelength.

Table of Contents

List of Figures

List of Tables

Chapter 1 Introduction

1.1 Motivation

The National Science Foundation (NSF) has recognized the need for optical scientists and engineers to improve the power and efficiency of the National Information Infrastructure (NII).[1] Just this May, Gary Bjorklund, the President of the Optical Society of America, spoke at the University of Rochester's Institute of Optics and reiterated that the NSF recognizes the need for technological advances in optical communications. As computers become, more and more, a staple of our society, the information contained by them is increasing to a point where present state-of-the-art communication technology will be overcome by the quest for data. Communication systems depend on reliable device technologies. Devices, in turn, rely on "building block" structures. This thesis addresses the modeling and fabrication of a structure, the optically-resonant periodic electrode (ORPEL) structure, which can be a building block for a variety of wavelength-selective, active optoelectronic components.

1.2 Current Trends

Optical and optoelectronic communications are experiencing unprecedented growth. One development that has fueled this growth is the upgrade of older long-haul, single wavelength systems to ones which carry multiple wavelengths over single-mode fibers (wavelength-division multiplexing). For WDM-based long-haul systems, standards and components are already well-established. This is due to the fact that fiber investment dwarfs terminal costs, and expensive terminal equipment is still highly cost effective. The latter is not the case for optical communications networks, so there is

still a need for additional research and development of cost-effective components for WDM networking.

Communication between electronic components is also a technological area in need of breakthrough improvements prior to full realization of the National Information Infrastructure (NII). In the ever-expanding field of communications, much has been written and reported on the need for free-space optical interconnects that can be mass produced and compatible with present VLSI technology.[2] At present, performance of complex integrated circuits is limited by the number of wires capable of connecting one component to another. The efficient production of silicon based, VLSI-compatible optoelectronic modulators would therefore have a tremendous impact on the NII.

Wavelength-selective detectors and wavelength-selective optical switches/ modulators[3-4] are two classes of components which, if integrated with low-cost electronics, could provide a major reduction in cost of WDM networking components. VLSI compatibility is an important goal for any such class of devices, and it is therefore interesting to examine their capabilities in respect to a silicon-based materials system.

There are three wavelength regimes in which silicon-based devices might play a role. Optical data storage systems, as well as some network connections, use short wavelength (< 850 nm) semiconductor lasers and silicon detectors. Current WDM systems, as well as other long-haul technologies, operate around the 1550 nm range which corresponds to the gain region of Erbium-doped fiber amplifiers and the lowest loss region of silica fiber. Finally, low-cost diode-pumped solid state lasers (Nd:YAG and Nd:YLF) operate near 1060 nm, corresponding closely to the indirect band-edge of silicon. It is at this last wavelength that most all-optical switching experiments in silicon have been performed.

Consensus is growing that there is a critical need for the realization of an efficient all-optical switch. Such a device could replace certain electronic switches in logic (i.e., multiplexing and demultiplexing) operations and in fiber optic applications would eliminate the need for optoelectronic signal conversion. While neither an ideal material nor a device structure has yet proved viable, it is clear from early work in optoelectronics, that any "all-optical" technology will likely need some form of electronic control mechanism. The study of a class of optical switching devices which naturally incorporate an electrode structure is therefore an important, and useful, pursuit.

1.3 Background

In previous work, several groups have explored the properties of a class of structures referred to as guided-mode resonant filters.[5-8] They have shown that planar dielectric diffraction gratings can theoretically exhibit narrow linewidth ($\Delta\lambda \approx 0.01$ nm) resonances. Their work concentrated on structures exhibiting complete energy exchange between 0^{th} order reflectance and transmitance. Possible applications of such filters include line narrowing of laser cavities and electro-optic logic switches. Norton, Erdogan and Morris published a detailed experimental study of dielectric structures.[7-8]

Rochester-based studies of optical switching in nonlinear media have used both corrugated waveguides[9-10] and periodic-electrode structures[11-13] as the optical coupling mechanism. Figure 1.1 illustrates a generic ORPEL structure which from the top view looks like an interdigitated MSM circuit element, but in cross section, provides a structure which is an optical resonator.

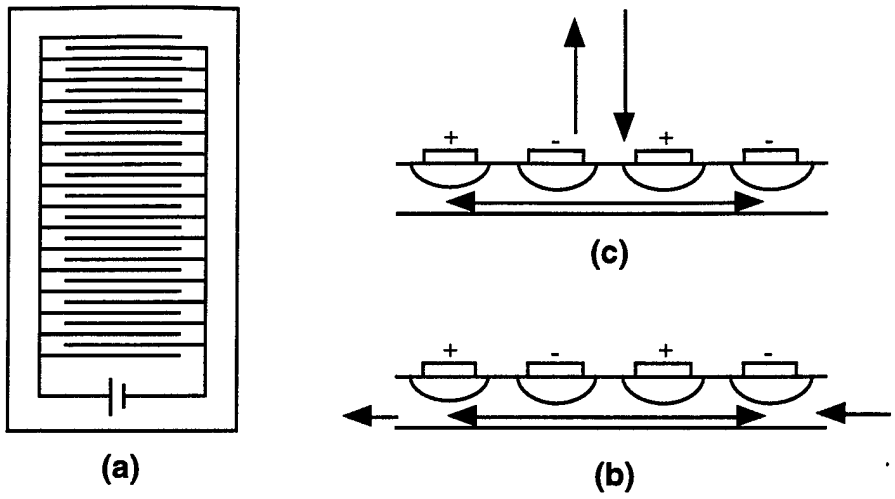

Figure 1.1 - ORPEL Structure
(a) top view, (b) side view - illustrating in-plane coupling, and (c) side view - illustrating out-of-plane coupling

Two generic switching geometries can be employed. The first geometry (figure 1.1b), termed the "in-plane" switching geometry, describes those cases in which light switches between guided modes of the structure. These geometries were studied by Sankey et al. (for corrugated structures) and by Bieber et al. (for ORPEL structures). For in-plane coupling, a forward-traveling mode couples into its backward-traveling counterpart. The second geometry (figure 1.1c), which we will refer to as the "out-of-plane" coupling geometry, describes the resonant interaction of a radiation mode (cover or substrate) and a guided mode. Both geometries can be the basis for either optoelectronic modulation (electronic control of an optical beam) or all-optical switching.

In-plane switching in a silicon-on-insulator (SOI) structure was first demonstrated by Sankey, Prelewitz, and Brown.[9-10,14] Prior to this work, research in the area of nonlinear periodic structures was mostly theoretical. Following this effort, Bieber, Prelewitz and Brown successfully achieved all-optical switching by overlaying a metal-

semiconductor-metal (MSM) structure over the SOI waveguide.[11-13] The use of the MSM coupler provides the properties necessary to electronically control the properties of the switch. It is this combination of interdigitated metallic fingers upon a silicon waveguide that is referred to as an optically-resonant periodic electrode (ORPEL) structure.

In addition to detecting and switching applications, periodic waveguides may also function as polarizers. Since TE and TM mode resonances may occur at different wavelengths, it is possible to envision the use of such structures as wavelength-selective polarizers.[5]

Rigorous solution of Maxwell's Equations allow diffracted waves to be analyzed exactly, but calculations are often labor intensive. The development of coupled-wave theory has served well as an analytical tool. Most recently, the formulation of rigorous coupled-wave theory in a simple matrix form has placed this analysis within the reach of desktop computers.[15-16]

1.4 Outline

The goal of this work was to further model and optimize ORPEL structures designed for out-of-plane switching, detection, or modulation. In doing so, we have pulled together, for the first time, two ongoing efforts. Bieber et al. successfully demonstrated coupling and switching in ORPEL structures but stopped short of optimization. Peng efficiently analyzed periodic structures through rigorous coupled-wave analysis and, thereby, provided the tool necessary to effectively model these structures. The marriage of these two efforts, along with the introduction of design

optimization, was the next logical step in the Institute of Optics' ongoing research in the field of integrated optoelectronics and diffractive optics.

Since the methods used to provide first-order off-resonance design do not work well for the modeling of TM-polarized light, the modeling and optimization presented in this research is limited to ORPEL structures' response to TE-polarized light. This inability to accurately produce an initial TM-polarized model is in part due to the discontinuity in the electric field caused by the geometry of the metallic grating.

This thesis consists of three major sections. Chapter 2 begins with a discussion and overview of the structures under study and concludes by describing the techniques used for modeling and optimization. Among its appendices is a catalog of optimized designs for three wavelength regimes. Chapter 3 contains a description of the procedures used to fabricate and characterize these structures and some experimental results are presented. Finally, in chapter 4, the optical characterization of fabricated models are presented and discussed.

Chapter 2 Modeling and Optimization

2.1 Description of Structures

The structures modeled and optimized for this work consist of a silicon-on-insulator (SOI) base, upon which a metal grating is formed and an amorphous silicon (α-Si) overlayer deposited. Being silicon-based, these structures are compatible, in principle, with modern VLSI systems. This compatibility is crucial to the eventual integration of optical and optoelectronic devices into existing semiconductor applications.

Silicon-on-insulator (SOI) materials were used as the foundation for building the optically resonant periodic electrode (ORPEL) structures. The use of SOI structures as waveguides has been previously demonstrated.[17-18] In a SOI structure (figure 2.1), wave propagation occurs in a silicon layer that is separated from the silicon substrate by a sufficiently thick insulator (usually an oxide or nitride of silicon).

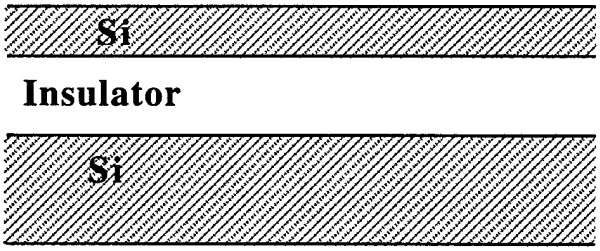

Figure 2.1 - SOI structure

The periodic grating of the ORPEL structure serves as the optical coupler required to achieve the selected mode of the waveguide. Through diffraction, the grating couples incident light into the waveguide, and after some amount of propagation, the wave is coupled out of the waveguide as either a reflected or transmitted wave. This creates a waveguide resonance that allows an otherwise highly reflective structure to

either transmit or absorb the incident light. By changing the grating period we can selectively "tune" the waveguide to the desired resonant wavelength. Such gratings are commonly produced using electron-beam lithography, deposition, and metal lift-off techniques. For this work, such techniques were not readily available, so alternative procedures were used. The details of these are discussed in Chapter 3.

The amorphous silicon overlayer serves two purposes. First, it adds a degree of freedom to the structure by allowing the grating to be floated at various depths during optimization. Secondly, by allowing the metal grating to be buried within a nearly continuous semiconductor layer, efficient waveguide coupling is achieved by providing increased overlap between the metal and waveguide modes.[11] Additionally, the amorphous silicon overlayer provides protection to a very fragile metallic grating. This is important as the grating structure has sub-wavelength characteristics in both period and depth.

2.2 Design

The modeling and optimization of the ORPEL structures was conducted using a four-step design sequence. The first step in the process was to calculate thicknesses in order to maximize the off-resonant reflectance. These initial thicknesses were then modeled using rigorous coupled-wave analysis over a broad range of wavelengths, and a resonant mode chosen for further investigation. The selected mode was then shifted to match the design wavelength by adjusting the grating period of the structure. Finally, optimization of the mode was performed by altering layer thicknesses to minimize a pre-defined merit function. This optimization step took various routes depending on the design. Ultimately, an optimized design was produced.

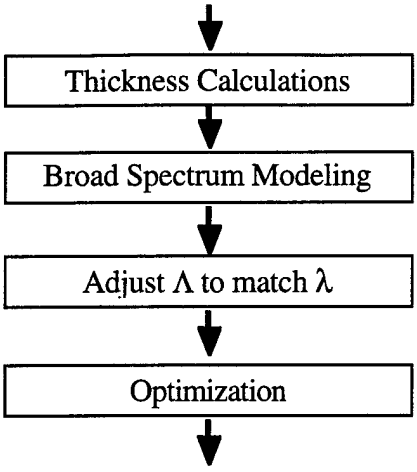

Figure 2.2 - Design Sequence

In order to best take advantage of a resonant wavelength, the structure needs to be designed to provide maximum off-resonance reflectance, and thereby achieve the greatest contrast between the off- and on-resonance condition. Since the structures contain a metallic grating, the initial design needs to maximize both the metallic and non-metallic regions. For the purpose of illustration, appendix 2A contains the calculations necessary to arrive at these first-order results. Table 2.1 lists the optical constants used throughout this research.[19]

Material	0.820 μm	**1.064 μm**	**1.550 μm**
Silicon (Si)	3.678+0.004i	3.53	3.476
Silicon Dioxide (SiO_2)	1.453	1.45	1.444
Amorphous Silicon (α-Si)	3.664	3.602	3.48
Gold (Au)	0.186+5.322i	0.285+7.354i	0.559+9.81i

Table 2.1 - Optical constants of materials used in this study[19]
The complex refractive index is given in the form n + ik, with the n denoting the dispersive part of the refractive index and k denoting the extinction coefficient

For an ORPEL structure containing a gold grating and designed for a resonant wavelength of $\lambda = 1.064$ μm, the set of overcoat, waveguide, and insulator layer thicknesses shown in table 2.2 are calculated to provide maximum off-resonance reflectance. Since the calculated thickness of each layer is independent of any other layer, any combination of three should provide an adequate starting point for further investigation. Figure 2.3 shows two such combinations ready for modeling and optimization and will be used as examples throughout the rest of this chapter.

α-Si (μm)	Si (μm)	SiO_2 (μm)
0.124	0.098	0.183
0.270	0.249	0.549
0.416	0.399	0.915
0.562	0.550	1.281
0.708	0.701	1.647

Table 2.2 - Off-resonance design thicknesses

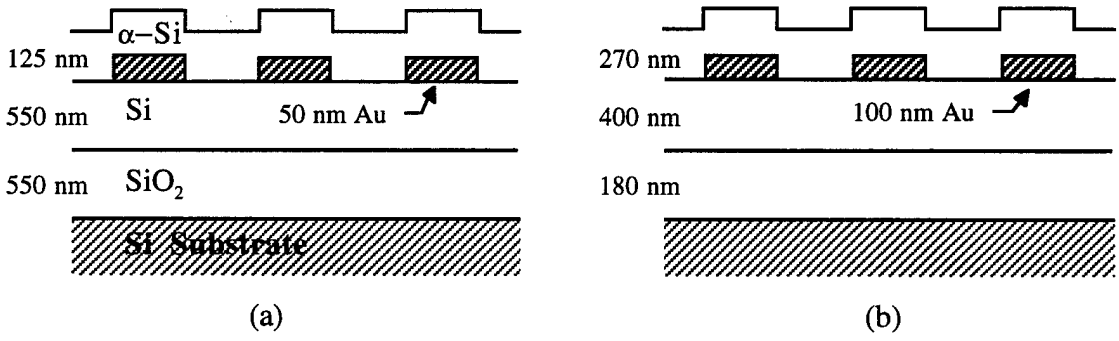

Figure 2.3 - First-order designs for maximum off-resonant reflectance

The initial analysis of the structure does not include a thickness of the metallic grating itself. The reason is as follows: After round-trip attenuation, the strength of the reflected wave from the lower surface of a 50 nm gold film (k=7.354 at 1.064 mm) is of the order 10^{-4}. So, a 50 nm film or thicker is adequate for first order modeling of off-resonance reflectance. The impact of the finite thickness of the metal is included when rigorous analysis is used during optimization.

These calculations serve as a first-order design for any given set of optical constants and can be easily modified to provide a minimum off-resonance reflectance if the intended application dictates. Due to the large quantity of thickness options associated with any given solution, the task of initial design becomes somewhat cumbersome without automation. Therefore, a spreadsheet was developed during the course of this research to return the set of thicknesses available for any combination of optical constants. An example of this spreadsheet is included as appendix 2B.

Once the first-order design is accomplished, the structure can be analyzed through rigorous numerical methods; the grating period can, in turn, be adjusted to tune the structure's resonance to a particular target wavelength.

2.3 Rigorous Model

The programs used to perform modeling and optimization were written on the MATLAB™ platform, a matrix-based technical computing environment. The original programs, written by Dr. Song Peng, use efficient, rigorous coupled-wave methods to analyze surface-relief gratings.[15-16] The user input includes scalar values for wavelength, period, duty cycle, angle of incidence, polarization, incident and substrate refractive indices, grating refractive indices, grating depth, and the number of diffraction orders retained. To model more complex (multilayer or non-binary)

profiles, the grating's thickness, high and low indices, and duty cycle may be provided as an input matrix. In such cases, each matrix row represents a single sub-layer of the structure. The resulting output provides reflection and transmission diffraction efficiencies for each order retained as well as total absorption. Appendix 2C contains examples and explanations of typical user input, as well as their corresponding results.

The program had the capability to vary any one scalar grating parameter over a user-defined range and step size. The programs, in their original form, however, lacked the ability to vary either elements of the matrix-defined profile or two grating parameters at one time. To use this already available and efficient software as an optimizer, it was necessary to modify the programs to allow matrix and multiple parameter variations.

Since the methods used to provide a first-order off-resonance design only work well for predicting TE-polarized light, modeling and optimization presented in this research must be limited to an ORPEL structure's response to TE-polarized light. The inability to accurately produce an initial TM-polarized model is in part due to the discontinuity in the electric field caused by the periodic nature of the structure. In terms of grating geometry, shown in figure 2.4, a non-conical mount (δ=0) is therefore assumed. Additionally, incident light is assumed to be a plane wave.

All grating profiles were assumed to be rectangular. This assumption was necessary because the profile of fabricated gratings was unknown at the time of optimization. Therefore, both the metallic grating and overcoat-air interface layers were modeled with rectangular profiles. The software has the capability to split any lamellar grating into a chosen number of layers. By this means, a trapezoidal or sinusoidally corrugated grating could be modeled as a finite number of rectangular sub-layers. The effect of such modeling is discussed in the work of Peng and Morris.[16]

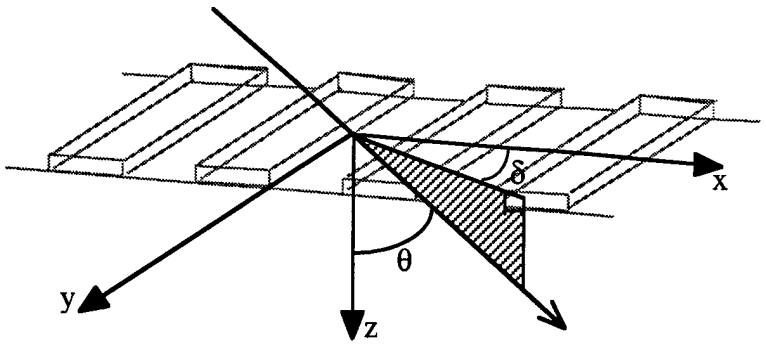

Figure 2.4 - Grating geometry

Gratings were also assumed to have a half-period duty-cycle. This eliminates one degree of freedom from the optimization process. The effects of a deviation of the duty cycle from 0.5 are discussed in chapter 3.

Each starting design was modeled by rigorous coupled-wave analysis using a trial grating period. The grating period was then adjusted to bring the resonance anomaly to the target wavelength. The calculated results of the starting designs (calculated and shown earlier) appear in figures 2.5 and 2.6. Similar figures are used throughout this paper. The 0^{th} order graph plots the reflection and transmission diffraction efficiencies (represented by the dark solid and light dashed lines, respectively) of normally incident light (θ=0). The +1 and -1 diffraction orders are similarly depicted. The lower right-hand plot shows total absorption in the analyzed structure. Finally, the hash marks appearing on the 0^{th} order reflection plot represent the peak reflectance locations on either side of the resonance, and the higher of the two is additionally indicated by a circle.

In the structure with the 550 nm waveguide layer (figure 2.5), we see that the first-order design has produced a very high off-resonance reflectance (0.95). Additionally, the resonance is already very deep (minimum reflectance < .01) and somewhat sharp

(linewidth ≈ 5.2 nm). On the other hand, the 400 nm design lacks these characteristics (maximum reflectance = 0.92, minimum reflectance = 0.19, and linewidth ≈ 11 nm).

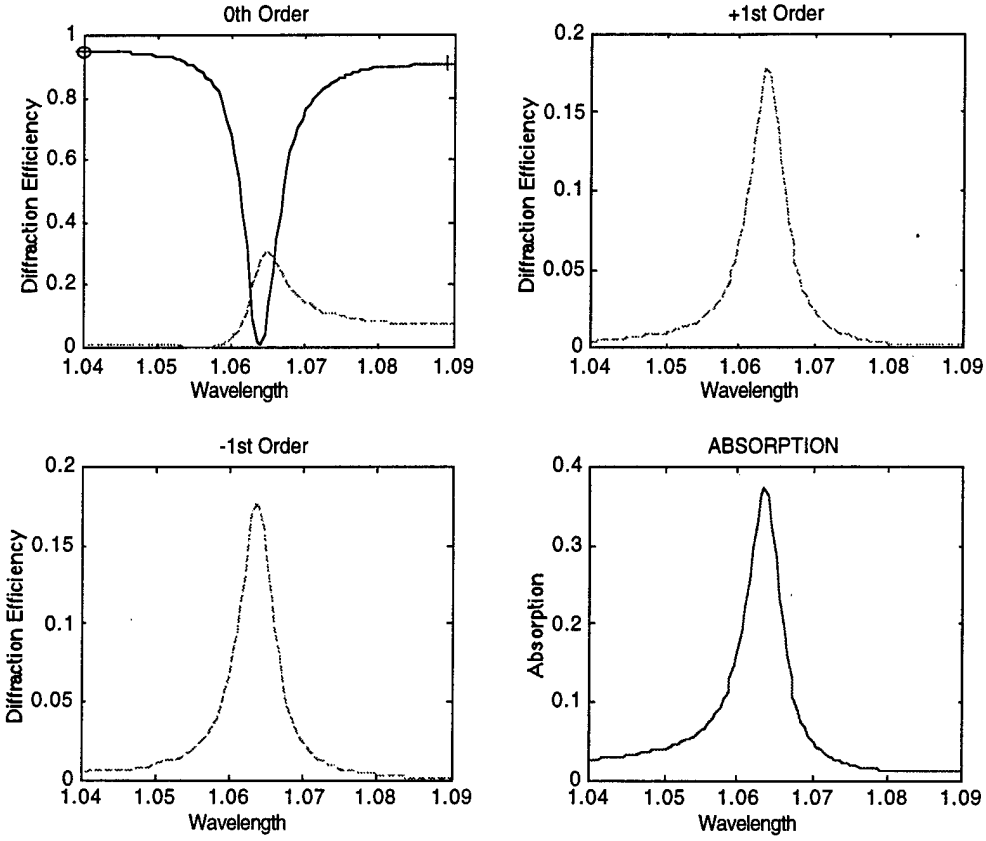

Figure 2.5 - Rigorous results of ORPEL structure following first-order design (550 nm SiO_2, 550 nm Si, 50 nm Au, 125 nm α-Si, and 734 nm grating period)

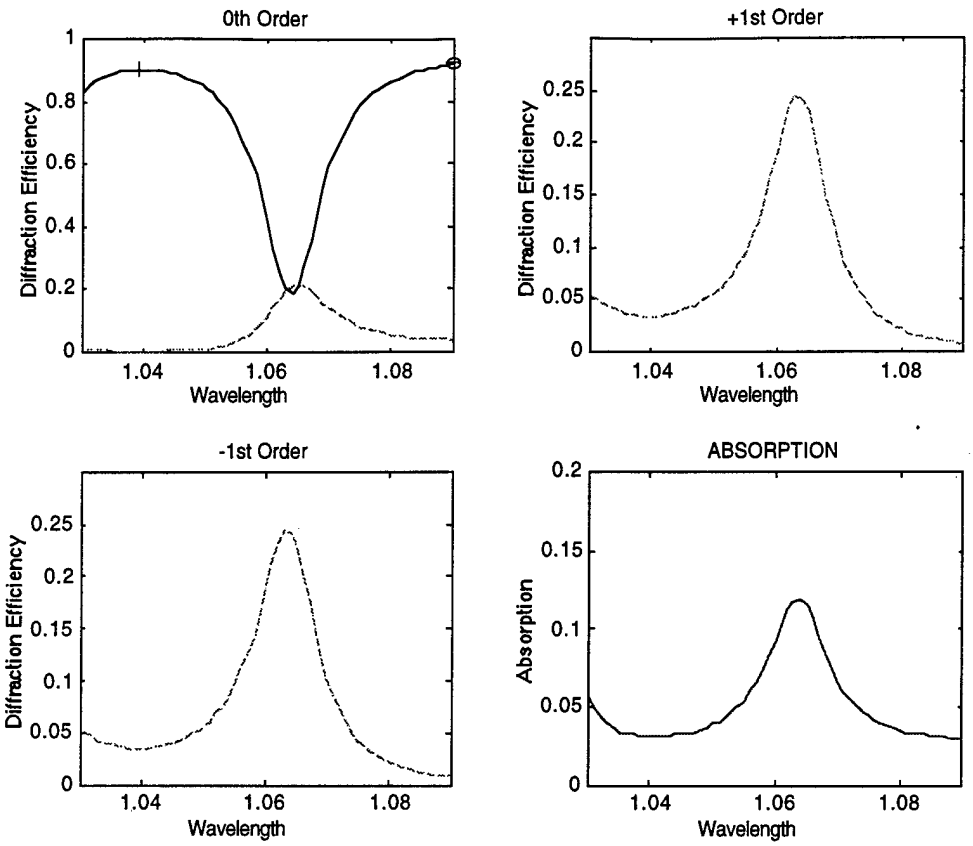

Figure 2.6 - Rigorous results of ORPEL structure following first-order design (180 nm SiO_2, 400 nm Si, 100 nm Au, 270 nm α-Si, and 677 nm grating period)

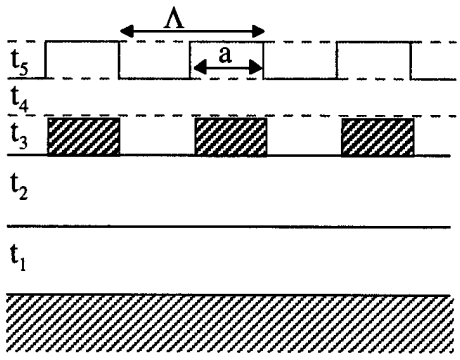

Figure 2.7 - ORPEL structure
(The dark hashed regions correspond to a buried metal electrode structure.)

2.4 Optimization

Optimization is the progression from an initial design to an optimum one, and must consider the structure's eventual application. The characteristics of a good optical switch are not necessarily those desired in a detector, or vise versa. In order to achieve optimization, a scalar merit function must first be developed to measure the quality of the design. Then, adjustments to the design may be evaluated.

An example of the ORPEL structure in figure 2.7, suggests that optimization is difficult, at best, due to the large number of degrees of freedom. At minimum, we have a five layer structure: insulator (t_1), cover (t_2), metallic grating (t_3), continuous overcoat (t_4), and overcoat-air grating (t_5). Additionally, the period (Λ), duty cycle (a/Λ), and cross-sectional shape of the grating can further complicate optimization. As stated previously, we are assuming a rectangular grating profile, and the grating period simply shifts the wavelength of the resonance. The profile and period are therefore not considered free parameters in the optimization.

Optimization is performed by incrementally changing thicknesses of the various layers in the structure. Since any change in thickness alters the resonance wavelength, adjustment of the grating period is necessary prior to evaluating the effect of each step. Once tuned to match the design wavelength, the model's figures of merit and merit function are re-calculated and compared with the previous value.

Depending on the application desired for an ORPEL structure, numerous possible figures of merit emerge. For the optimization associated with this research the following values were used. They are illustrated graphically in figure 2.8.

1) Maximum Reflectance (R_{MAX}). The peak off-resonant reflectance. Ideally R_{MAX} = 1.0, but a benchmark of 0.95 was established.

2) Minimum Reflectance (R_{MIN}). The reflectance at the resonant wavelength. Ideally, $R_{MIN} = 0.0$, but a benchmark of 0.05 was established.

3) Slope Efficiency (SE). Defined as the rate of change in reflectance to change in wavelength multiplied by the average wavelength.

$$SE = \left| \frac{(R_{90} - R_{10})}{\Delta\lambda} \right| \times \frac{(\lambda_{90} + \lambda_{10})}{2} \tag{2.1}$$

The "90" and "10" subscripts denote the 90% and 10% points between R_{MAX} and R_{MIN}, as illustrated in figure 2.8. For both Maximum Reflectance and Slope Efficiency, two possible values exist, one on either side of the resonant wavelength.

4) Linewidth (LW) and Linewidth Efficiency (LW_{EFF}). Linewidth is the full width at half-maximum of the resonance, and Linewidth Efficiency is the Linewidth divided by resonant wavelength.

$$LW_{EFF} = \frac{(\lambda_{50}^{+} - \lambda_{50}^{-})}{\lambda} \tag{2.2}$$

Figure 2.8 shows an example of these figures of merit.

As a benchmark, if we propose a λ=1.064 μm resonance with a 0.05 minimum reflectance, an off-resonance reflectivity of 0.95, and a required wavelength shift of 4 nm to switch between the 10% and 90% points of the resonance, we can calculate the following.

$$\frac{R_{MIN}}{R_{MAX}} = 5.26 \times 10^{-2} \tag{2.3}$$

$$\frac{1}{SE} = 5.22 \times 10^{-3} \tag{2.4}$$

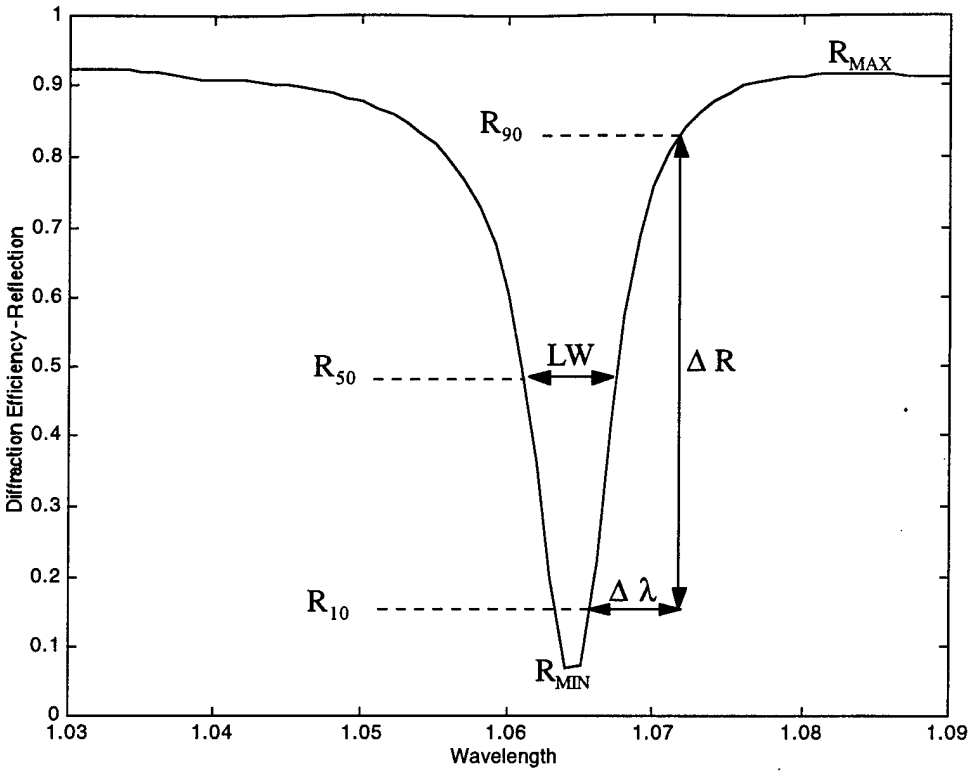

Figure 2.8 - Graphical depiction of figures of merit

We see that for our benchmark resonance, equation 2.3 is a single order of magnitude greater than the equation 2.4, which suggests the use of the following merit function.

$$\text{Optimization Value (OPTval)} = \frac{R_{MIN}}{R_{MAX}} + \frac{10}{SE} \qquad (2.5)$$

By including the factor of ten in the second half of the equation, both terms now contribute equally to the optimization value. This prevents either term from disproportionately contributing to any optimization sequence at the expense of the other. Finally, our benchmark resonance has an optimization value of 1.05×10^{-1}.

The first sequence in figure 2.9 incrementally steps each layer thickness toward a decreasing merit function independent of the remaining four. This is performed by finding the direction of decreasing merit function for each layer and then changing all five thicknesses simultaneously until a local minimum is reached. At that time, the optimizing direction is recalculated, with step directions being reversed where necessary. This method allows the structure to quickly minimize the merit function. Once reached, the resulting thicknesses can either be used as the optimized design or used as a starting point for further optimization. Appendix 2D contains mathematical expressions illustrating this five-variable optimization sequence. Since both grating layers (metallic and overcoat/air interface) are optimized independently of one another, this sequence allows their final thicknesses to differ. With more sophisticated fabrication techniques, one would be able to take full advantage of this additional degree of freedom. Since present fabrication methods deposit the overcoat uniformly over the entire metallic grating layer, optimized designs presented in this research were restricted to having equal grating thicknesses ($t_3 = t_5$). However, this optimization sequence was frequently used since it often proved to be the quickest route to an improved design. If a pair of unequal thicknesses is produced ($t_3 \neq t_5$), both are adjusted to their midpoint, and thereby, the total thickness of the multilayer is not altered.

Because fabrication for this research was limited to the SOI structures already on-hand, the optimization of the insulator and waveguide layers (figure 2.9's 2nd, 3rd, and 6th sequences) were not always performed. In the development of designs to be fabricated and experimentally characterized, optimization was limited to the metallic grating and the overcoat layer thicknesses. Therefore, appendix 2E (Catalog of optimized designs) contains three types of structures: unlimited designs, where each layer of the structure may be of any thickness; conformal overcoat designs, with equal

grating and overcoat/air interface thicknesses; and fabrication designs, with pre-determined SOI thicknesses. One of the design wavelengths, 1550 nm, lent itself well to a hybrid of the latter two levels of optimization. An investigation of published optical constants indicated that the refractive indices for silicon and amorphous silicon converge at approximately 1550 nm. Since we had the capability to deposit an amorphous silicon overlayer, we could likewise deposit an underlayer prior to metal deposition and thus enable an additional degree of freedom (t_2) to be optimized while only slightly modifying the fabrication process.

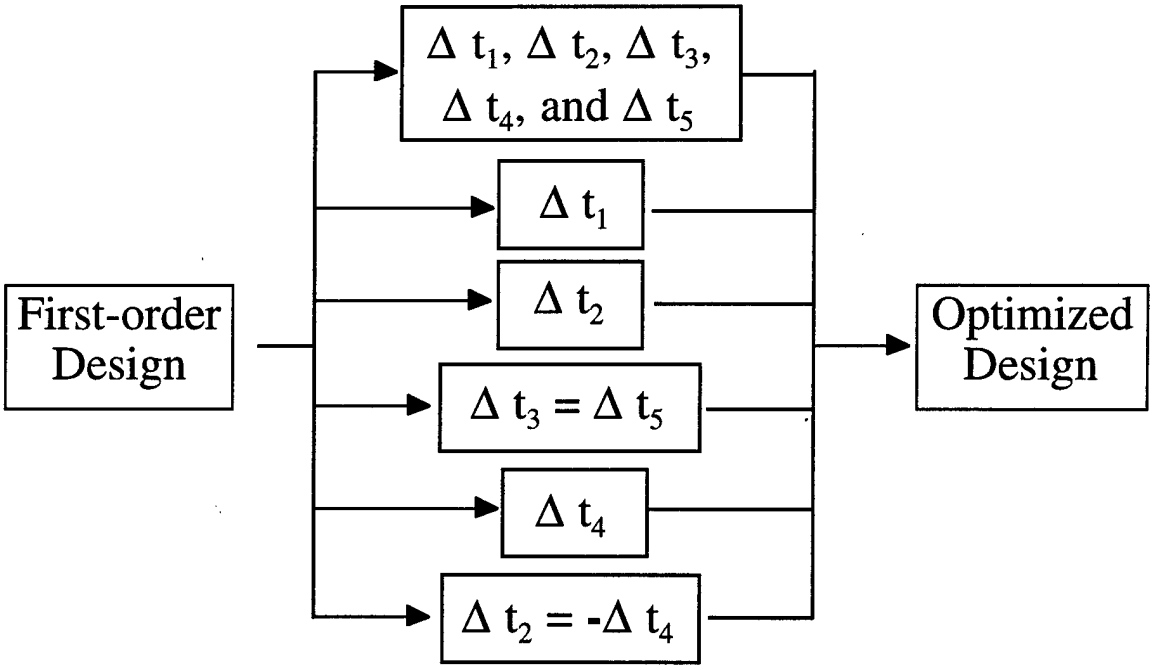

Figure 2.9 - The various optimization routes used during this research

Following rigorous analysis, it is interesting to take a look at how a particular first-order design evolved into an optimized model. In the $\lambda = 1.064$ μm design (figure 2.10 and table 2.3), we see that the initial first-order model undergoes negligible

improvement if optimization is constrained by available SOI wafers. Not only are both adjustable thicknesses changed less than 4 nm, but the merit function is only improved by 1%. If we include the SOI structure as free parameters, the resulting optimized design shows an improvement of greater than 50% from its initial design. The design progression of the 1550 nm model (figure 2.11 and table 2.4) clearly shows value of the optimization process. From first-order design to complete optimization, we have a three-fold increase in contrast between on- and off-resonance reflectances and the merit function has improved by 84%. Additionally, the resonances linewidth has narrowed to less than 1 nm.

Once satisfied that a particular model has been optimized to a sufficient level, the fabrication process may begin.

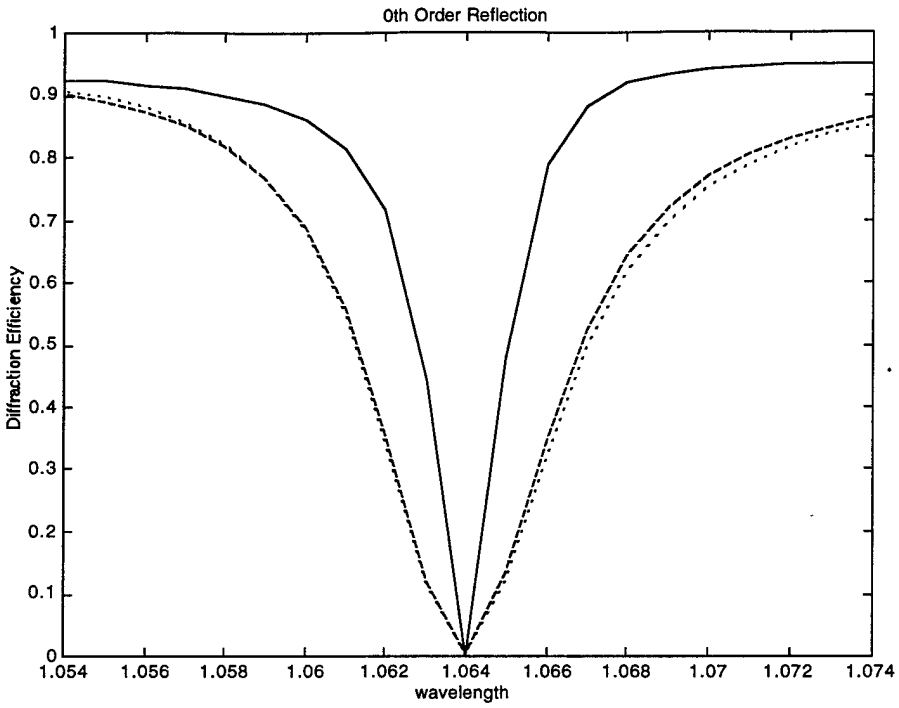

Figure 2.10 - Rigorous results of a first-order design at 1.064 μm (dotted), with its subsequent partially optimized (dashed) and optimized (solid) designs.

Design Level	SiO_2 (μm)	Si (μm)	Au (μm)	a-Si (μm)	Λ (μm)	OPTval
First-order	0.550	0.550	0.050	0.125	0.7342	0.0797
Partially Optimized	0.550	0.550	0.048	0.121	0.7413	0.0789
Optimized	0.542	0.578	0.043	0.109	0.6849	0.0371

Table 2.3 - Layer thicknesses, grating periods, and merit functions (OPTval) of 1.064 μm structures in figure 2.10

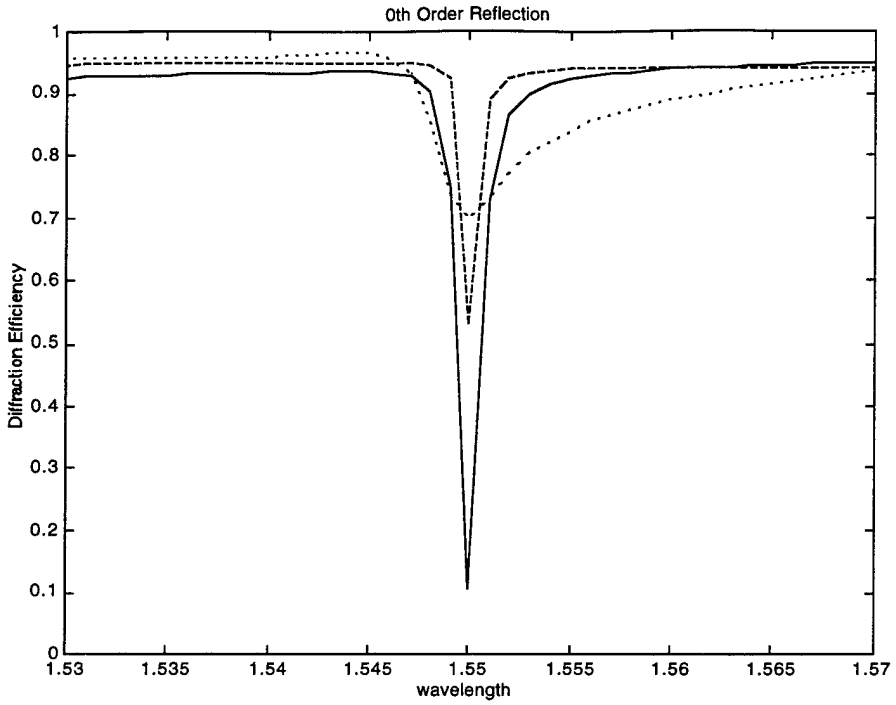

Figure 2.11 - Rigorous results of a first-order design at 1.550 μm (dotted), with its subsequent partially optimized (dashed) and optimized (solid) designs.

Design Level	SiO_2 (μm)	Si (μm)	Au (μm)	a-Si (μm)	Λ (μm)	OPTval
First-order	1.000	2.500	0.100	0.200	0.8340	0.7920
Partially Optimized	1.040	2.300	0.069	0.191	0.7946	0.5932
Optimized	1.040	2.440	0.089	0.178	0.8950	0.1292

Table 2.4 - Layer thicknesses, grating periods, and merit functions (OPTval) of 1.550 μm structures in figure 2.11

Appendix 2A Sample Off-Resonance Calculation

The phase shift upon reflection from the amorphous silicon-gold interface can be found as follows ($n_1 = n_{\alpha-Si} = 3.65$ and $n_2 = n_{Au} = 0.285 + 7.35i$):

$$r = \frac{n_1 - n_2}{n_1 + n_2} = \frac{-40.782 - 53.655i}{69.507} \tag{2A.1}$$

$$\phi = \tan^{-1}\left(\frac{r_{imaginary}}{r_{real}}\right) = \pi + 0.92 \text{ radians} \tag{2A.2}$$

In the metallic region of the grating,

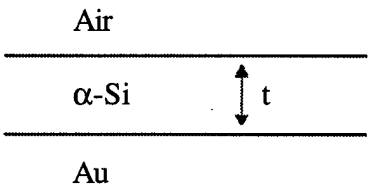

we can determine the thickness of the amorphous silicon overcoat that will yield a maximum reflectance. This occurs when the round-trip phase shift is an odd multiple of π.

$$\phi + \frac{2\pi}{\lambda}(2nt) = (2j+1)\pi \tag{2A.3}$$

(ϕ is the phase shift due to the gold interface - calculated above, t is the thickness of the α–Si overcoat, and n is the refractive index for α–Si)

Solving for t,

$$t = 2.32 \times 10^{-2}\ \mu m\ (2\pi j - 0.92) \qquad (2A.4)$$

results in a set of possible amorphous silicon thicknesses.

j	t (μm)
1	0.124
2	0.270
3	0.416
4	0.562
5	0.708

By designing the structure using a noble metal of sufficient thickness, we are able to neglect the reflection associated with the metal-silicon interface at the bottom surface of the grating. (Due to the high absorption, a thickness of approximately 50 nm significantly attenuates any reflected wave.)

In the non-metallic region of the grating, we can similarly determine the thickness of silicon that will produce a maximum reflectance.

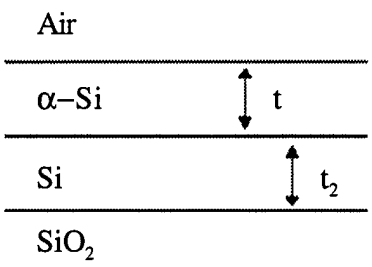

Using the α–Si thickness (t) calculated for the metallic region, maximum reflectance again occurs when the round-trip phase shift is an odd multiple of π.

$$\frac{2\pi}{\lambda}\left(2nt + 2t_2 n_2\right) = (2j+1)\pi \qquad (2A.5)$$

(t_2 is the thickness of the Si layer, and n_2 is the refractive index of Si)

Solving for t_2, we find that

$$t_2 = \frac{1}{13.271}(2j+1) - 1.034t, \qquad (2A.6)$$

which provides the following set of solutions:

j t	0.124	0.270	0.416	0.562
1	0.098			
2	0.249	0.098		
3	0.399	0.248	0.097	
4	0.550	0.399	0.248	0.097

The final layer of the structure can now be modeled.

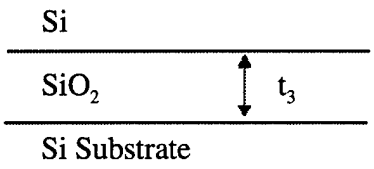

We can determine the thickness of the insulator layer that will yield constructive reflection. Again, this occurs when the round-trip phase shift is an odd multiple of π.

$$\frac{2\pi}{\lambda}\left(2t_3 n_3\right) = (2j+1)\pi \qquad (2A.7)$$

(t_3 and n_3 are the thickness and refractive index of SiO_2, respectively)

Solving for t_3, we find that

$$t_3 = 0.183\mu m\,(2j+1), \qquad (2A.8)$$

which provides the following set of solutions:

j	$t_3(\mu m)$
1	0.183
2	0.549
3	0.915
4	1.281
5	1.647

Appendix 2B Off-Resonance Design Spreadsheet

		n						thickness (μm)		options
	layer	1.00		air						
							0.063			
	3	3.600		α-Si			0.063			
		.285+7.354i		Au			0.063	0.1263863	0.0524974	1
	2	3.53		Si				0.5492943	0.5492943	4
	1	1.450		SiO2				0.5503448	0.3668965	1
		3.678+.004i		Si				MAX refl.	MIN refl.	

nmetal	.285+7.354i	0.285+7.354i		r=	-0.595631577808373-0.765437677425283i					
n3	3.600	3.6								
n2	3.530	3.53		ϕ=	4.0511					
n1	1.450	1.45								
λ	1.064									
		j3	t3min	t3max						
		1	0.052497464	0.126386353						
		2	0.200275242	0.274164131						
		3	0.348053020	0.421941909						
		4	0.495830798	0.569719687						
		5	0.643608575	0.717497464						

	j2 \ t3min						j2 \ t3min	
		0.052497464	0.200275242	0.348053020	0.495830798	0.643608575		0.0524974
	1	0.097169724	-0.053538490	-0.204246706	-0.354954921	-0.505663136	1	0.0971697
	2	0.247877939	0.097169724	-0.053538490	-0.204246706	-0.354954921	2	0.2478779
t2min =	3	0.398586154	0.247877939	0.097169724	-0.053538490	-0.204246706	3	0.3985861
	4	0.549294370	0.398586154	0.247877939	0.097169724	-0.053538490	4	0.5492943
	5	0.700002585	0.549294370	0.398586154	0.247877939	0.097169724	5	0.7000025
	6	0.850710800	0.700002585	0.549294370	0.398586154	0.247877939	6	0.8507108
	7	1.001419016	0.850710800	0.700002585	0.549294370	0.398586154	7	1.0014190
	8	1.152127231	1.001419016	0.850710800	0.700002585	0.549294370	8	1.1521272
	9	1.302835446	1.152127231	1.001419016	0.850710800	0.700002585	9	1.3028354
	10	1.453543661	1.302835446	1.152127231	1.001419016	0.850710800	10	1.4535436
	11	1.604251877	1.453543661	1.302835446	1.152127231	1.001419016	11	1.6042518
	12	1.754960092	1.604251877	1.453543661	1.302835446	1.152127231	12	1.7549600
	13	1.905668307	1.754960092	1.604251877	1.453543661	1.302835446	13	1.9056683
	14	2.056376523	1.905668307	1.754960092	1.604251877	1.453543661	14	2.0563765
	15	2.207084738	2.056376523	1.905668307	1.754960092	1.604251877	15	2.2070847
	16	2.357792953	2.207084738	2.056376523	1.905668307	1.754960092	16	2.3577929
	17	2.508501169	2.357792953	2.207084738	2.056376523	1.905668307	17	2.5085011
	18	2.659209384	2.508501169	2.357792953	2.207084738	2.056376523	18	2.6592093
	19	2.809917599	2.659209384	2.508501169	2.357792953	2.207084738	19	2.8099175
	20	2.960625814	2.809917599	2.659209384	2.508501169	2.357792953	20	2.96062581
	j2 \ t3max	0.126386353	0.274164131	0.421941909	0.569719687	0.717497464	j2 \ t3max	0.1263863
	1	0.097169724	-0.053538490	-0.204246706	-0.354954921	-0.505663136	1	0.0971697
	2	0.247877939	0.097169724	-0.053538490	-0.204246706	-0.354954921	2	0.2478779
t2max =	3	0.398586154	0.247877939	0.097169724	-0.053538490	-0.204246706	3	0.3985861
	4	0.549294370	0.398586154	0.247877939	0.097169724	-0.053538490	4	0.5492943
	5	0.700002585	0.549294370	0.398586154	0.247877939	0.097169724	5	0.7000025
	6	0.850710800	0.700002585	0.549294370	0.398586154	0.247877939	6	0.8507108
	7	1.001419016	0.850710800	0.700002585	0.549294370	0.398586154	7	1.0014190
	8	1.152127231	1.001419016	0.850710800	0.700002585	0.549294370	8	1.1521272
	9	1.302835446	1.152127231	1.001419016	0.850710800	0.700002585	9	1.3028354
	10	1.453543661	1.302835446	1.152127231	1.001419016	0.850710800	10	1.4535436
	11	1.604251877	1.453543661	1.302835446	1.152127231	1.001419016	11	1.6042518
	12	1.754960092	1.604251877	1.453543661	1.302835446	1.152127231	12	1.7549600
	13	1.905668307	1.754960092	1.604251877	1.453543661	1.302835446	13	1.9056683
	14	2.056376523	1.905668307	1.754960092	1.604251877	1.453543661	14	2.0563765
	15	2.207084738	2.056376523	1.905668307	1.754960092	1.604251877	15	2.2070847
	16	2.357792953	2.207084738	2.056376523	1.905668307	1.754960092	16	2.3577929
	17	2.508501169	2.357792953	2.207084738	2.056376523	1.905668307	17	2.5085011
	18	2.659209384	2.508501169	2.357792953	2.207084738	2.056376523	18	2.6592093
	19	2.809917599	2.659209384	2.508501169	2.357792953	2.207084738	19	2.8099175
	20	2.960625814	2.809917599	2.659209384	2.508501169	2.357792953	20	2.96062581
	21	3.111334030	2.960625814	2.809917599	2.659209384	2.508501169	21	3.1113340
	22	3.262042245	3.111334030	2.960625814	2.809917599	2.659209384	22	3.2620422
	23	3.412750460	3.262042245	3.111334030	2.960625814	2.809917599	23	3.4127504
							t1min =	0.3668965
							t1max =	0.5503448

Appendix 2C Notes on the RCWA Software

Example of Input

Program prompts indicated by *italic* text.

beyond_mlt
Enter the index of the incident medium, substrate, high index of the grating, low index of the grating, wavelength, grating period, depth, duty cycle(length of the high index part over the period),incident angle(in degree), lower limit of the diffraction order, upper limit of the order, angle psi(90 for TE), and angle delta.

The default grating data is [1 3.53 1.5 1 1.064 .5 1 .5 0 -5 5 90 0].

If you need change the above data enter it in the same format(with [and] at each end), otherwise press RETURN.
[1 3.53 3.60 .285-7.35i 1.064 .734 1 .5 0 -5 5 90 0]

n_inc = 1.0000 0.0000i
n_sub = 3.5300 0.0000i
n_hgh = 3.6000 0.0000i
n_low = 0.2850 -7.3500i
wavelength = 1.0640
period = 0.7340
depth = 1.0000
dutycycle = 0.5000
theta = 0.0000
order_low = -5
order_hgh = 5
psi = 90.0000
delta = 0.0000
TE POLARIZATION NONCONICAL MOUNT

The above data may be changed to loop through ONE of the grating parameter. For example, typing "theta = 0:5:30;" provides data from normal incidence to 30 degree incidence with increment of 5 degree

ENTER the index PROFILE_MLT, the layer THICKNESS_MLT, and INDEXRFR_MLT.

Type in for example order_file=[-1:1]; to save the results of -1 to +1 orders in file. Type in store = n to skip file output.

Type in film = n to use same n_hgh and n_low for all layers.

After changing grating parameters, type "return" to start calculation.

```
THICKNESS_MLT=[.55;.55;.05;.075;.05];
PROFILE_MLT=[0 1;0 1;0 .5;0 1;0 .5];
INDEXRFR_MLT=[1.45 0;3.53 0;3.60 .285-7.354i;3.60 0;1 3.60];
wavelength=1.020:.001:1.095;
return
```

Author's notes concerning input:

Matrices are entered bound by brackets, rows are separated by semicolons, and elements in rows are separated by a space. The first row represents the sub-layer immediately preceding the substrate (in our case - the SiO_2) and the final row represents the sub-layer adjacent to the incident medium (the α-Si/air interface).

The THICKNESS_MLT matrix is simply a column matrix designating each layer thickness. The i^{th} element of any INDEXRFR_MLT row is that layer's refractive index between the i^{th} and $i+1^{st}$ elements of its corresponding PROFILE_MLT row. The third row (bold in the example above) represents a gold grating (0.05 μm thick), where amorphous silicon (n=3.60) is present over half the period (0 to .5) and gold (n=0.285+7.354i) the remaining half (.5 to 1).

Example of Screen Output

```
Estimate completion in less than  1  minutes

Result saved in file GS_DATA.

The highest propagating order in this calculation is (+ or -)  2.

Minimum Reflection Efficiency of 0.005863 occurred at wavelength of 1.064000 um

Maximum Reflection Efficiency of 0.949627 occurred at wavelength of 1.034000 um
  Long wavelength side's Max Efficiency of  0.904735 at  1.089000 um

Slope efficiencies (short and long side) are 132.3090 and 107.5311 respectively
Line Width efficiency is 0.00495
10:1 switch efficiency is 0.00188

Optimization value of 0.08175
```

Example of File Output

The following data is written to a file named GS_DATA.

1/28/98 6:57pm

GRATING PARAMETER

Layer	Thickness	Transition points		n_high	n_low
5	0.0500	0.0000	0.5000	1.0000+ 0.0000i	3.6000+ 0.0000i
4	0.0750	0.0000	1.0000	3.6000+ 0.0000i	0.0000+ 0.0000i
3	0.0500	0.0000	0.5000	3.6000+ 0.0000i	0.2850+-7.3540i
2	0.5500	0.0000	1.0000	3.5300+ 0.0000i	0.0000+ 0.0000i
1	0.5500	0.0000	1.0000	1.4500+ 0.0000i	0.0000+ 0.0000i

n_inc 1.000000 + 0.000000i
n_sub 3.530000 + 0.000000i
n_hgh 3.600000 + 0.000000i
n_low 0.285000 + -7.350000i
wavelength(VARIED) 1.064000
period 0.734000
depth 1.000000
dutycycle(NA) 0.500000
theta 0.000000
order_low -5.000000
order_hgh 5.000000
psi 90.000000
delta 0.000000
POLARIZATION TE

Minimum Reflection Efficiency of 0.005863 occurred at wavelength of 1.064000 um
Maximum Reflection Efficiency of 0.949627 occurred at wavelength of 1.034000 um
Long wavelength side's Max Efficiency of 0.904735 at 1.089000 um
Slope efficiencies (short and long side) are 132.308968 and 107.531074 respectively
Optimization value of 0

Diffraction Efficiency -- REFLECTION

wavelength	-2	-1	0	1	2
1.020000	0.000000	0.000000	0.945951	0.000000	0.000000
1.021000	0.000000	0.000000	0.946480	0.000000	0.000000
1.022000	0.000000	0.000000	0.946961	0.000000	0.000000
1.023000	0.000000	0.000000	0.947396	0.000000	0.000000
1.024000	0.000000	0.000000	0.947790	0.000000	0.000000
1.025000	0.000000	0.000000	0.948145	0.000000	0.000000
1.026000	0.000000	0.000000	0.948461	0.000000	0.000000
1.027000	0.000000	0.000000	0.948741	0.000000	0.000000
1.028000	0.000000	0.000000	0.948984	0.000000	0.000000
1.029000	0.000000	0.000000	0.949191	0.000000	0.000000
1.030000	0.000000	0.000000	0.949359	0.000000	0.000000
1.031000	0.000000	0.000000	0.949489	0.000000	0.000000

1.032000	0.000000	0.000000	0.949579	0.000000	0.000000
1.033000	0.000000	0.000000	0.949626	0.000000	0.000000
1.034000	0.000000	0.000000	0.949627	0.000000	0.000000

Data intentionally omitted for λ=1.035 to 1.055

1.056000	0.000000	0.000000	0.878385	0.000000	0.000000
1.057000	0.000000	0.000000	0.853713	0.000000	0.000000
1.058000	0.000000	0.000000	0.817260	0.000000	0.000000
1.059000	0.000000	0.000000	0.761534	0.000000	0.000000
1.060000	0.000000	0.000000	0.673748	0.000000	0.000000
1.061000	0.000000	0.000000	0.534416	0.000000	0.000000
1.062000	0.000000	0.000000	0.327725	0.000000	0.000000
1.063000	0.000000	0.000000	0.097069	0.000000	0.000000
1.064000	0.000000	0.000000	0.005863	0.000000	0.000000
1.065000	0.000000	0.000000	0.136120	0.000000	0.000000
1.066000	0.000000	0.000000	0.342462	0.000000	0.000000
1.067000	0.000000	0.000000	0.511151	0.000000	0.000000
1.068000	0.000000	0.000000	0.627030	0.000000	0.000000
1.069000	0.000000	0.000000	0.704269	0.000000	0.000000
1.070000	0.000000	0.000000	0.756582	0.000000	0.000000
1.071000	0.000000	0.000000	0.793034	0.000000	0.000000
1.072000	0.000000	0.000000	0.819192	0.000000	0.000000
1.073000	0.000000	0.000000	0.838470	0.000000	0.000000
1.074000	0.000000	0.000000	0.853008	0.000000	0.000000
1.075000	0.000000	0.000000	0.864185	0.000000	0.000000
1.076000	0.000000	0.000000	0.872914	0.000000	0.000000
1.077000	0.000000	0.000000	0.879818	0.000000	0.000000

Data intentionally omitted for λ=1.078 to 1.088

1.089000	0.000000	0.000000	0.904735	0.000000	0.000000
1.090000	0.000000	0.000000	0.904658	0.000000	0.000000
1.091000	0.000000	0.000000	0.904404	0.000000	0.000000
1.092000	0.000000	0.000000	0.903984	0.000000	0.000000
1.093000	0.000000	0.000000	0.903406	0.000000	0.000000
1.094000	0.000000	0.000000	0.902676	0.000000	0.000000
1.095000	0.000000	0.000000	0.901800	0.000000	0.000000

Diffraction Efficiency -- TRANSMISSION

wavelength	-2	-1	0	1	2
1.020000	0.000000	0.003193	0.025156	0.003193	0.000000
1.021000	0.000000	0.003159	0.024627	0.003159	0.000000
1.022000	0.000000	0.003135	0.024109	0.003135	0.000000
1.023000	0.000000	0.003123	0.023600	0.003123	0.000000
1.024000	0.000000	0.003120	0.023099	0.003120	0.000000
1.025000	0.000000	0.003127	0.022606	0.003127	0.000000
1.026000	0.000000	0.003143	0.022119	0.003143	0.000000
1.027000	0.000000	0.003167	0.021637	0.003167	0.000000
1.028000	0.000000	0.003201	0.021158	0.003201	0.000000
1.029000	0.000000	0.003243	0.020681	0.003243	0.000000
1.030000	0.000000	0.003296	0.020204	0.003296	0.000000
1.031000	0.000000	0.003358	0.019726	0.003358	0.000000

1.032000	0.000000	0.003430	0.019245	0.003430	0.000000
1.033000	0.000000	0.003514	0.018760	0.003514	0.000000
1.034000	0.000000	0.003611	0.018267	0.003611	0.000000
Data intentionally omitted for λ=1.035 to 1.055					
1.056000	0.000000	0.023672	0.001681	0.023672	0.000000
1.057000	0.000000	0.029365	0.002320	0.029365	0.000000
1.058000	0.000000	0.037455	0.004909	0.037455	0.000000
1.059000	0.000000	0.049321	0.011426	0.049321	0.000000
1.060000	0.000000	0.067188	0.025908	0.067188	0.000000
1.061000	0.000000	0.094098	0.056273	0.094098	0.000000
1.062000	0.000000	0.131356	0.114873	0.131356	0.000000
1.063000	0.000000	0.168039	0.205191	0.168039	0.000000
1.064000	0.000000	0.173742	0.285677	0.173742	0.000000
1.065000	0.000000	0.139969	0.301076	0.139969	0.000000
1.066000	0.000000	0.097667	0.268486	0.097667	0.000000
1.067000	0.000000	0.065945	0.227271	0.065945	0.000000
1.068000	0.000000	0.045353	0.192840	0.045353	0.000000
1.069000	0.000000	0.032229	0.166803	0.032229	0.000000
1.070000	0.000000	0.023676	0.147439	0.023676	0.000000
1.071000	0.000000	0.017915	0.132910	0.017915	0.000000
1.072000	0.000000	0.013905	0.121834	0.013905	0.000000
1.073000	0.000000	0.011027	0.113251	0.011027	0.000000
1.074000	0.000000	0.008906	0.106503	0.008906	0.000000
1.075000	0.000000	0.007307	0.101135	0.007307	0.000000
1.076000	0.000000	0.006076	0.096826	0.006076	0.000000
1.077000	0.000000	0.005112	0.093346	0.005112	0.000000
Data intentionally omitted for λ=1.078 to 1.088					
1.089000	0.000000	0.001113	0.082035	0.001113	0.000000
1.090000	0.000000	0.001009	0.082450	0.001009	0.000000
1.091000	0.000000	0.000917	0.083002	0.000917	0.000000
1.092000	0.000000	0.000836	0.083686	0.000836	0.000000
1.093000	0.000000	0.000764	0.084500	0.000764	0.000000
1.094000	0.000000	0.000699	0.085440	0.000699	0.000000
1.095000	0.000000	0.000641	0.086505	0.000641	0.000000

TOTAL ABSORPTION AND/OR COMPUTATIONAL ERROR

wavelength	ABSORPTION
1.020000	2.250648e-02
1.021000	2.257529e-02
1.022000	2.265970e-02
1.023000	2.275823e-02
1.024000	2.287021e-02
1.025000	2.299554e-02
1.026000	2.313456e-02
1.027000	2.328796e-02
1.028000	2.345671e-02
1.029000	2.364210e-02
1.030000	2.384566e-02
1.031000	2.406923e-02

1.032000 2.431496e-02
1.033000 2.458538e-02
1.034000 2.488342e-02
Data intentionally omitted for λ=1.035 to 1.055
1.056000 7.259056e-02
1.057000 8.523750e-02
1.058000 1.029214e-01
1.059000 1.283986e-01
1.060000 1.659695e-01
1.061000 2.211159e-01
1.062000 2.946889e-01
1.063000 3.616626e-01
1.064000 3.609752e-01
1.065000 2.828662e-01
1.066000 1.937178e-01
1.067000 1.296875e-01
1.068000 8.942472e-02
1.069000 6.446976e-02
1.070000 4.862652e-02
1.071000 3.822493e-02
1.072000 3.116445e-02
1.073000 2.622480e-02
1.074000 2.267586e-02
1.075000 2.006634e-02
1.076000 1.810839e-02
1.077000 1.661301e-02
Data intentionally omitted for λ=1.078 to 1.088
1.089000 1.100315e-02
1.090000 1.087353e-02
1.091000 1.075927e-02
1.092000 1.065786e-02
1.093000 1.056724e-02
1.094000 1.048579e-02
1.095000 1.041223e-02

Appendix 2D Methodology of 5-Variable Optimization

The merit function, M, is evaluated for initial thicknesses, t_1 through t_5, and for independent steps, $t_i + \Delta t$.

$$M = M(t_1, t_2, t_3, t_4, t_5),$$

$$M_1 = M(t_1 + \Delta t, t_2, t_3, t_4, t_5),$$

$$M_2 = M(t_1, t_2 + \Delta t, t_3, t_4, t_5), \text{ and}$$

$$\vdots$$

$$M_5 = M(t_1, t_2, t_3, t_4, t_5 + \Delta t)$$

With these values, a vector defining the step direction is evaluated,

$$S_i = \text{sgn}(M - M_i), \text{ for } i = 1 \text{ to } 5$$

and steps continue in the direction of decreasing merit function.

$$M' = M(t_1 + S_1\Delta t, t_2 + S_2\Delta t, t_3 + S_3\Delta t, t_4 + S_4\Delta t, t_5 + S_5\Delta t)$$

If $M' < M$, the process continues.

If $M' > M$, then the sequence halts and returns the last set of thicknesses to the start point to begin the process again.

Appendix 2E Catalog of Optimized Designs

The following designs were among those optimized during the course of this research.

		wavelength	thickness (nm)				period
page	Figure	λ (nm)	SiO_2	Si	Au	α-Si	Λ (nm)
37	2E.1	1064	550	550	45	124	736.5
38	2E.2	1064	540	570	42	108	709.5
39	2E.3	1064	1040	2300	62	125	748.0
40	2E.4	1064	921	2359	72	135	735.5
41	2E.5	1550	550	550	70	231	610.0
42	2E.6	1550	1040	2440	89	178	895.0
43	2E.7	1550	730	476	114	197	686.0
44	2E.8	1550	789	563	104	218	605.5
45	2E.9	1550	799	809	102	218	647.0
46	2E.10	820	550	550	67	166	736.0
46	2E.11	820	1005	2287	109	237	678.0
47	2E.12	820	728	439	96	215	735.0
47	2E.13	820	730	460	97	194	735.5

Table 2E.1 - Reference List for Catalog of Optimized Designs

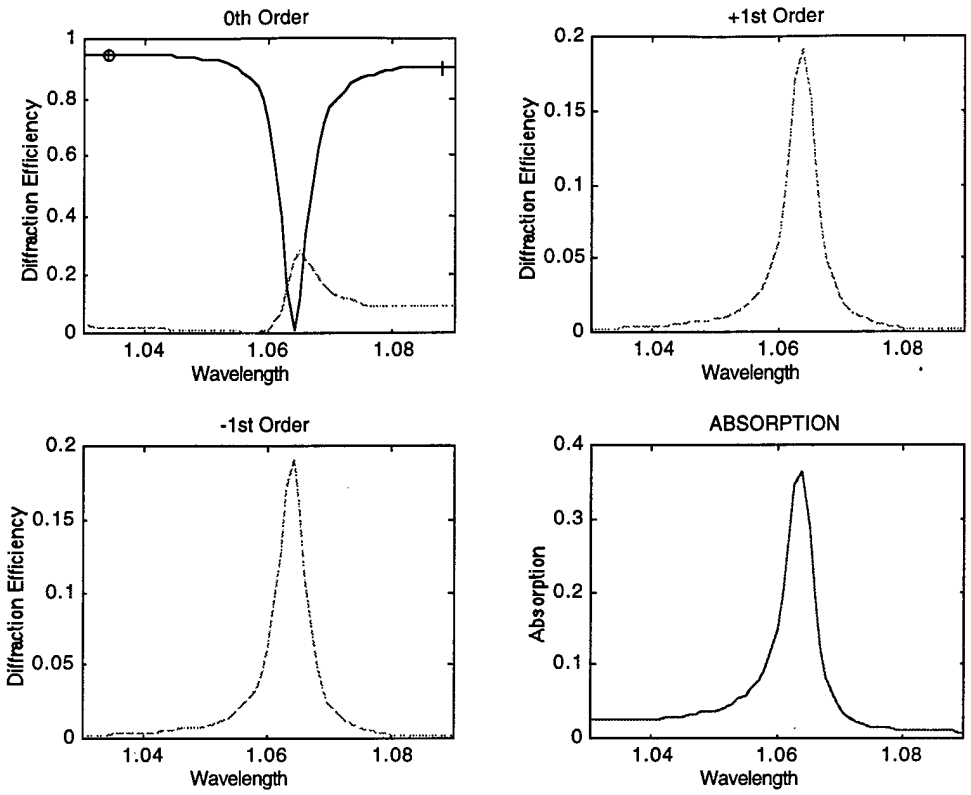

Figure 2E.1 - Optimized design for a $\lambda = 1.064$ μm resonance. Thicknesses: 550 nm SiO_2, 550 nm Si, 45 nm Au, and 124 nm α-Si $\Lambda = 736.5$ nm, $R_{MIN} = 0.0081$, $R_{MAX} = 0.9460$, LW = 5.1 nm

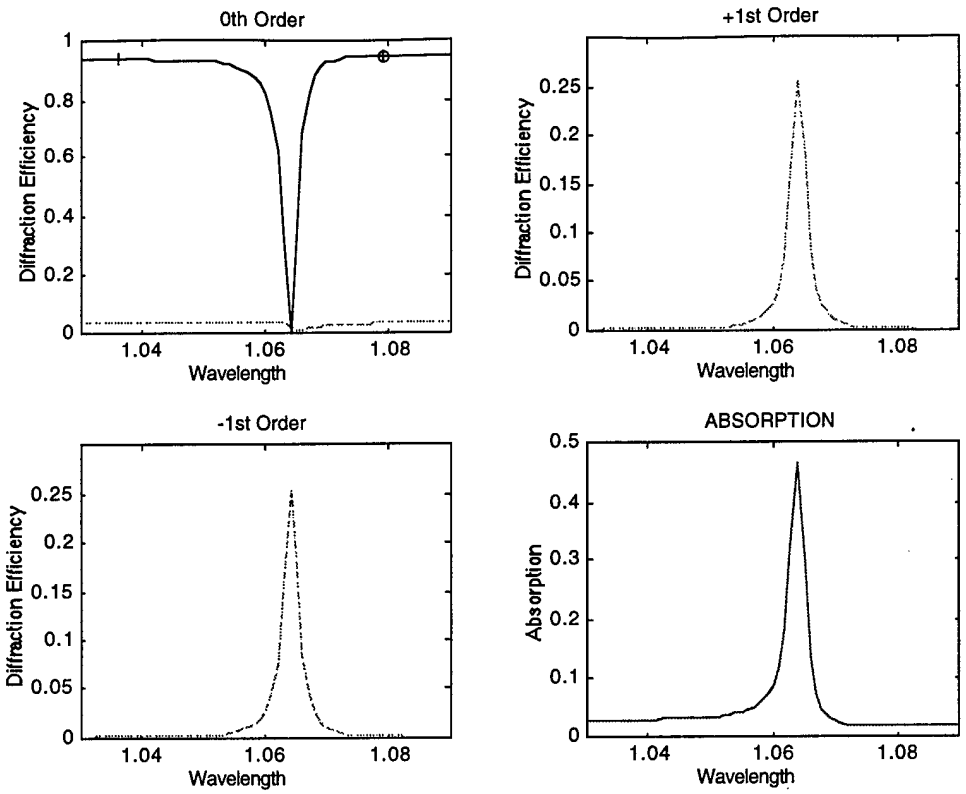

Figure 2E.2 - Optimized design for a $\lambda = 1.064$ μm resonance.
Thicknesses: 540 nm SiO_2, 570 nm Si, 42 nm Au, and 108 nm α-Si
$\Lambda = 709.5$ nm, $R_{MIN} = 0.0014$, $R_{MAX} = 0.9488$, LW = 2.7 nm

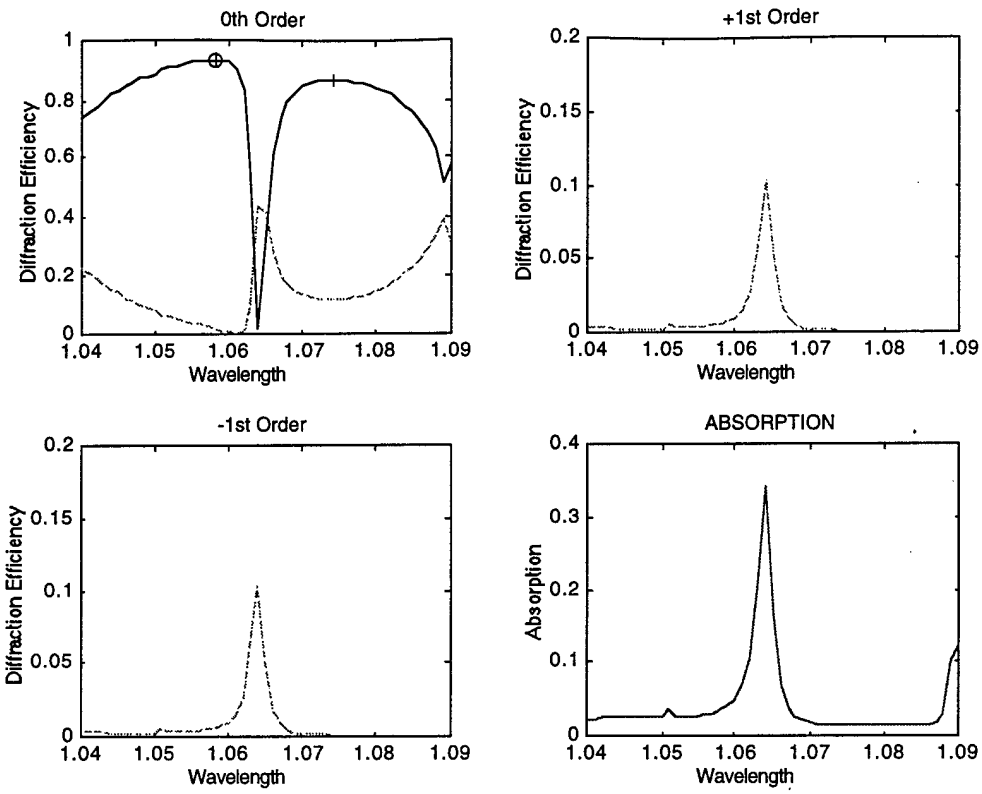

Figure 2E.3 - Optimized design for a λ = 1.064 μm resonance.
Thicknesses: 1.04 μm SiO_2, 2.30 μm Si, 62 nm Au, and 125 nm α-Si
Λ= 748 nm, R_{MIN} = 0.0175, R_{MAX} = 0.9321, LW = 2 nm

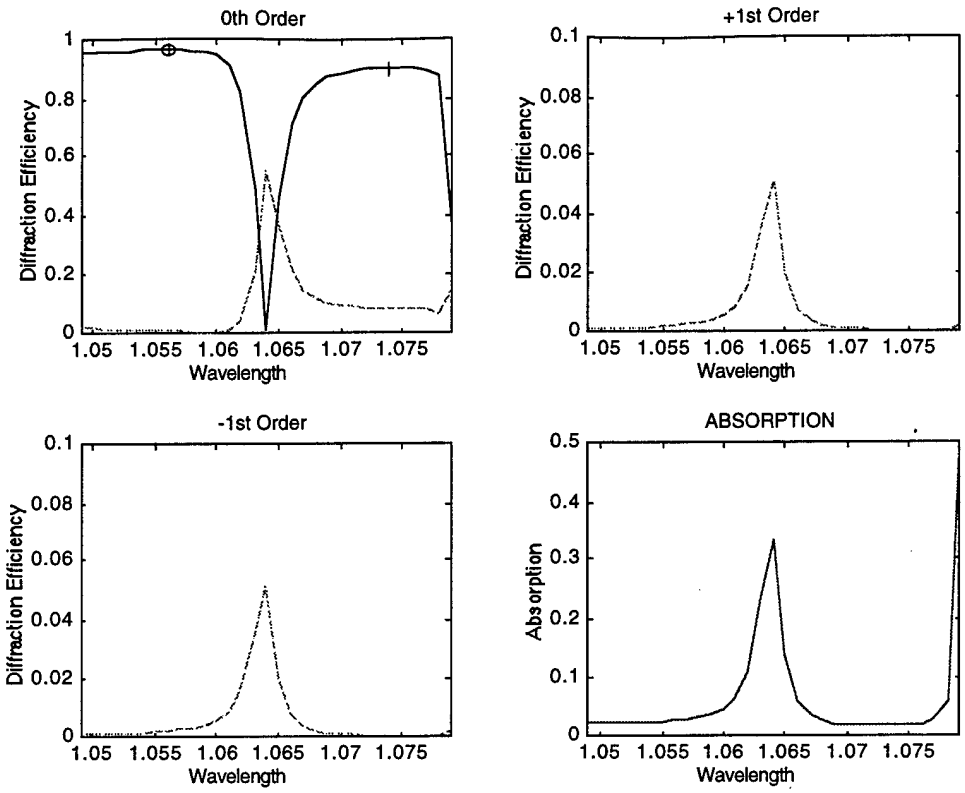

Figure 2E.4 - Optimized design for a $\lambda = 1.064$ μm resonance.
Thicknesses: 921 nm SiO_2, 2.359 μm Si, 72 nm Au, and 135 nm α-Si
$\Lambda = 735.6$ nm, $R_{MIN} = 0.0055$, $R_{MAX} = 0.9639$, LW = 2 nm

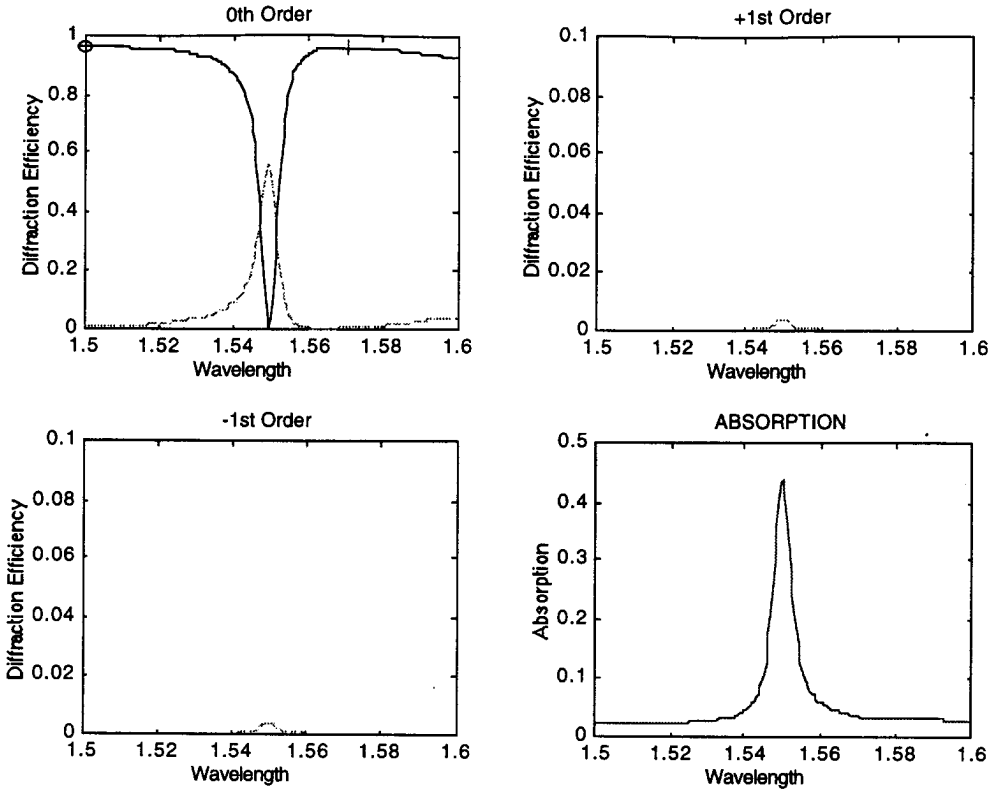

Figure 2E.5 - Optimized design for a λ = 1550 nm resonance.
Thicknesses: 550 nm SiO_2, 550 nm Si, 70 nm Au, and 231 nm α-Si
Λ= 610 nm, R_{MIN} = 0.00002, R_{MAX} = 0.9689, LW = 5.4 nm

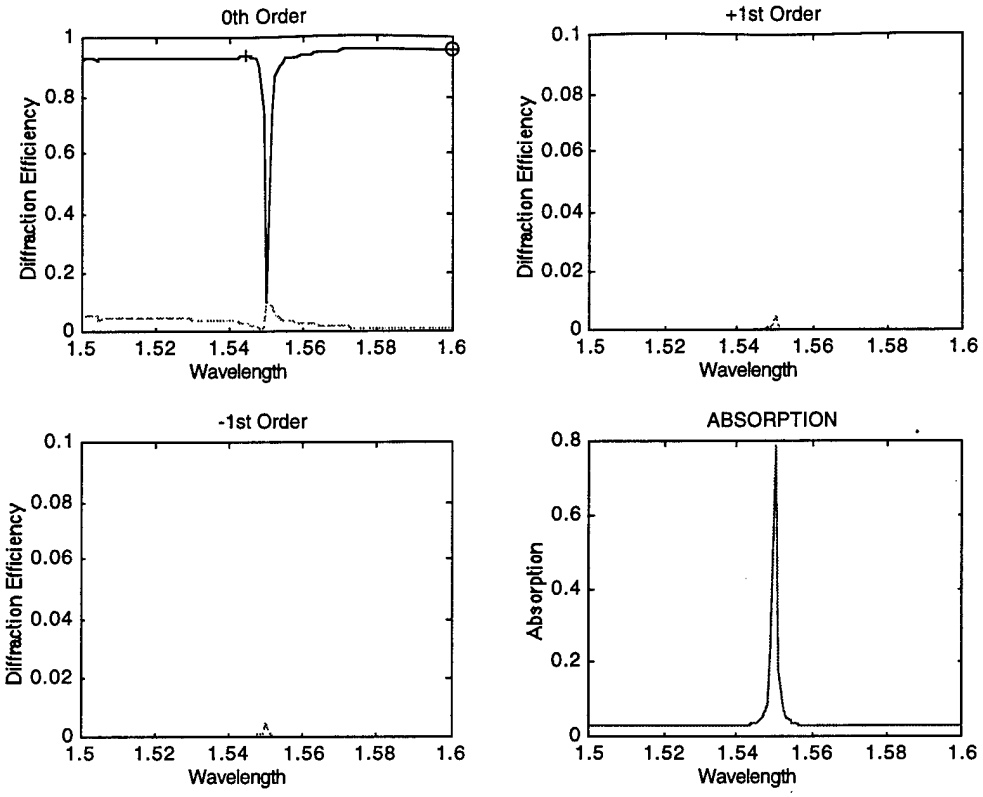

Figure 2E.6 - Optimized design for a λ = 1550 nm resonance.
Thicknesses: 1.04 μm SiO_2, 2.44 μm Si, 89 nm Au, and 178 nm α-Si
Λ= 895 nm, R_{MIN} = 0.1039, R_{MAX} = 0.9579, LW = 0.2 nm

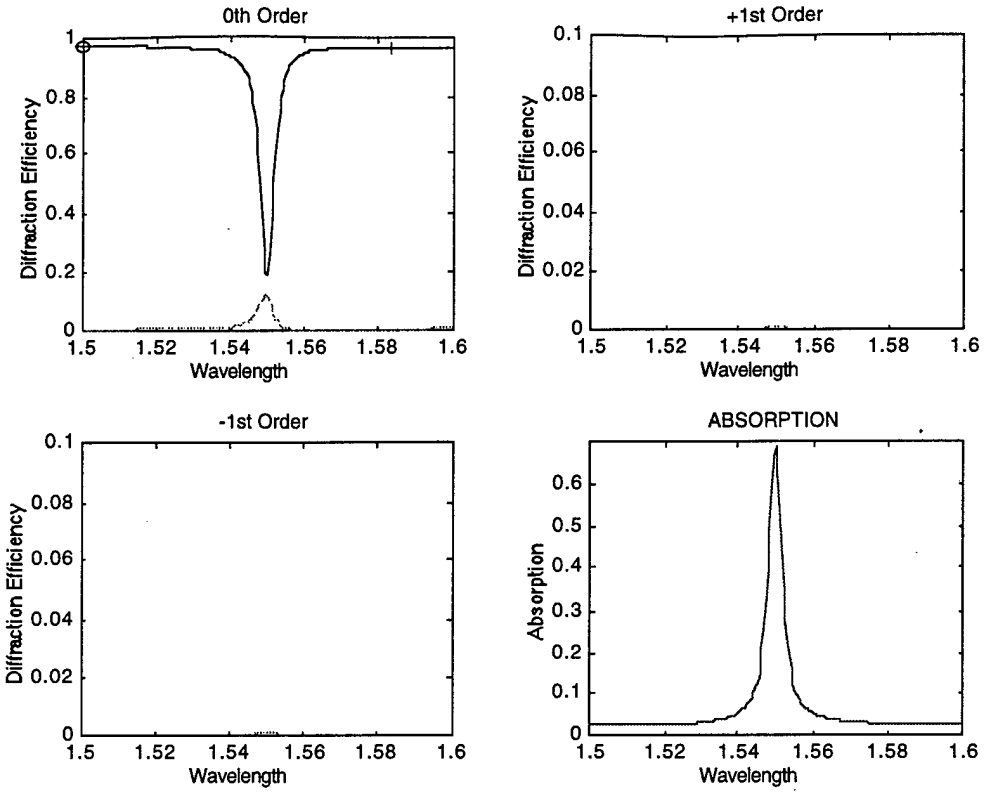

Figure 2E.7 - Optimized design for a λ = 1550 nm resonance.
Thicknesses: 730 nm SiO_2, 476 nm Si, 114 nm Au, and 197 nm α-Si
Λ= 686 nm, R_{MIN} = 0.1920, R_{MAX} = 0.9730, LW = 4.2 nm

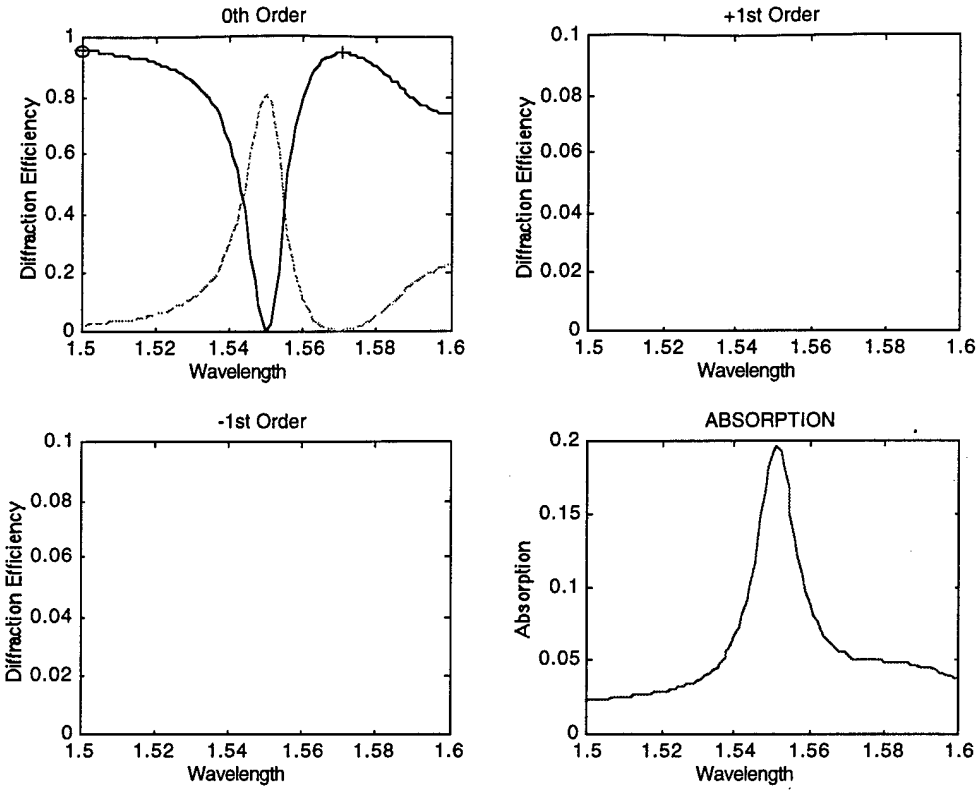

Figure 2E.8 - Optimized design for a λ = 1550 nm resonance.
Thicknesses: 789 nm SiO_2, 563 nm Si, 104 nm Au, and 218 nm α-Si
Λ= 605.5 nm, R_{MIN} = 0.0017, R_{MAX} = 0.9539, LW = 12 nm

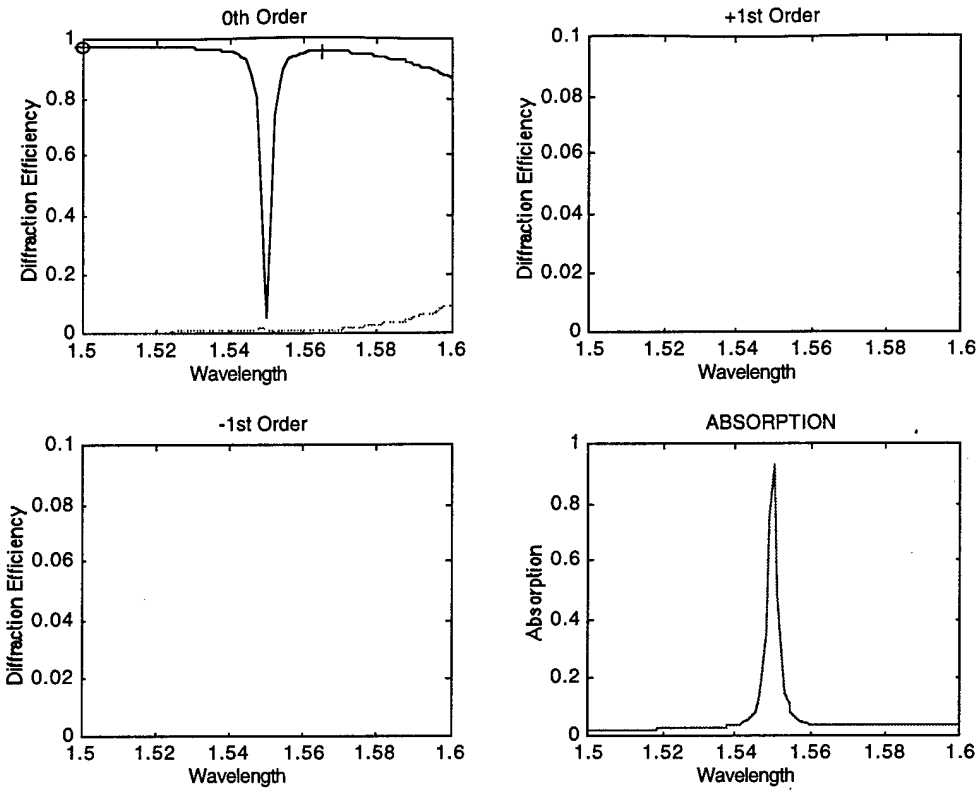

Figure 2E.9 - Optimized design for a λ = 1550 nm resonance.
Thicknesses: 799 nm SiO_2, 809 nm Si, 102 nm Au, and 218 nm α-Si
Λ= 647 nm, R_{MIN} = 0.0573, R_{MAX} = 0.9759, LW = 2.3 nm

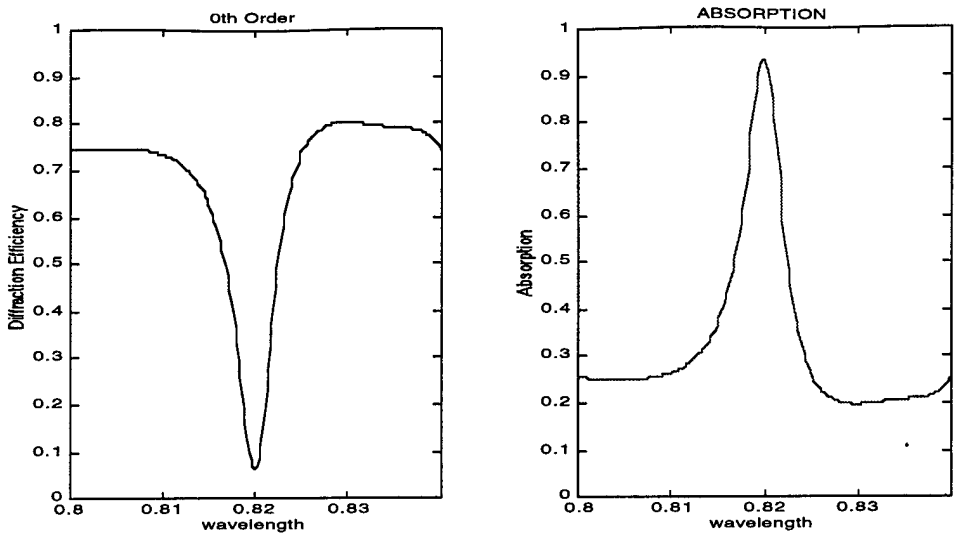

Figure 2E.10 - Optimized design for a λ = 820 nm resonance.
Thicknesses: 550 nm SiO_2, 550 nm Si, 67 nm Au, and 166 nm α-Si
Λ= 736 nm, R_{MIN} = 0.0652, R_{MAX} = 0.8028, LW = 4.6 nm

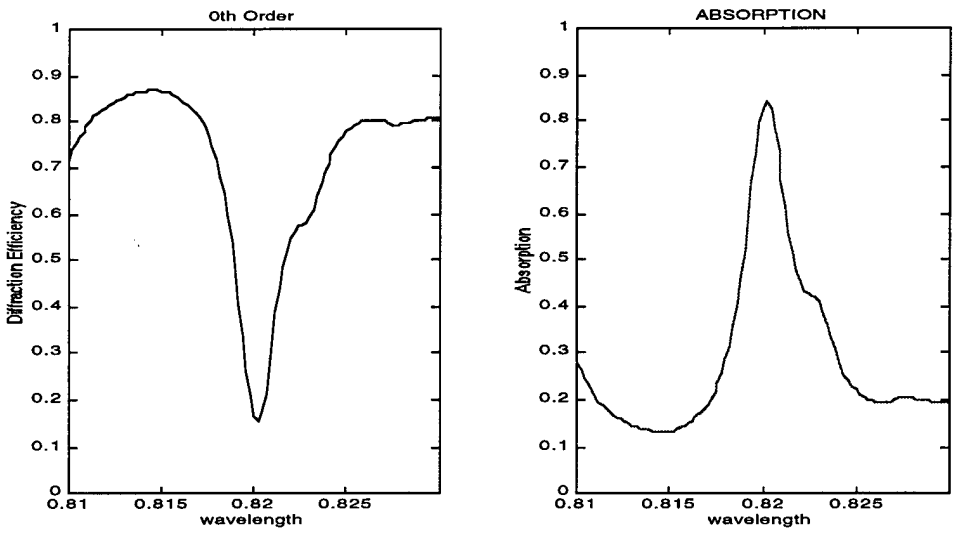

Figure 2E.11 - Optimized design for a λ = 820 nm resonance.
Thicknesses: 1.005 μm SiO_2, 2.287 μm Si, 109 nm Au, and 237 nm α-Si
Λ = 678 nm, R_{MIN} = 0.1555, R_{MAX} = 0.8683, LW = 2.8 nm

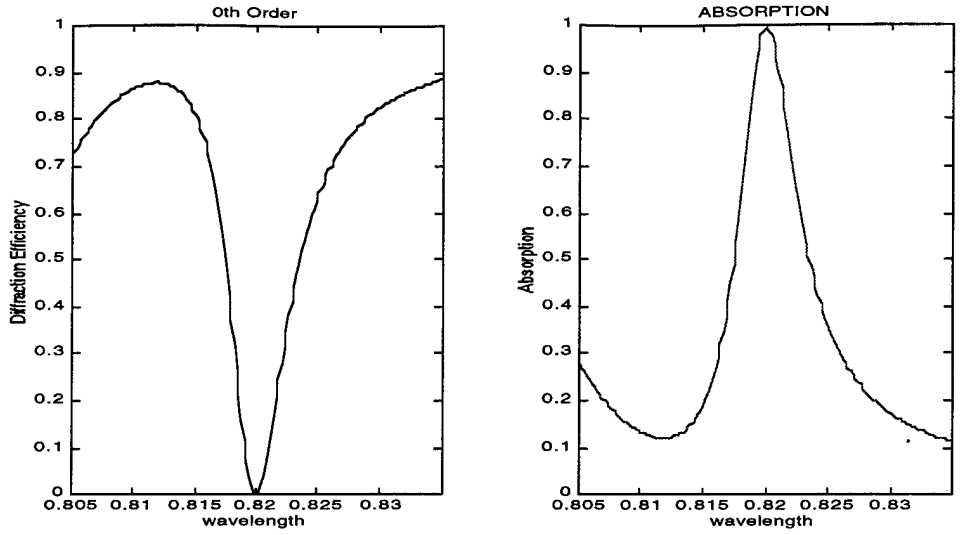

Figure 2E.12 - Optimized design for a λ = 820 nm resonance.
Thicknesses: 728 nm SiO_2, 439 nm Si, 96 nm Au, and 215 nm α-Si
Λ= 735 nm, R_{MIN} = 0.0040, R_{MAX} = 0.8868, LW = 5.3 nm

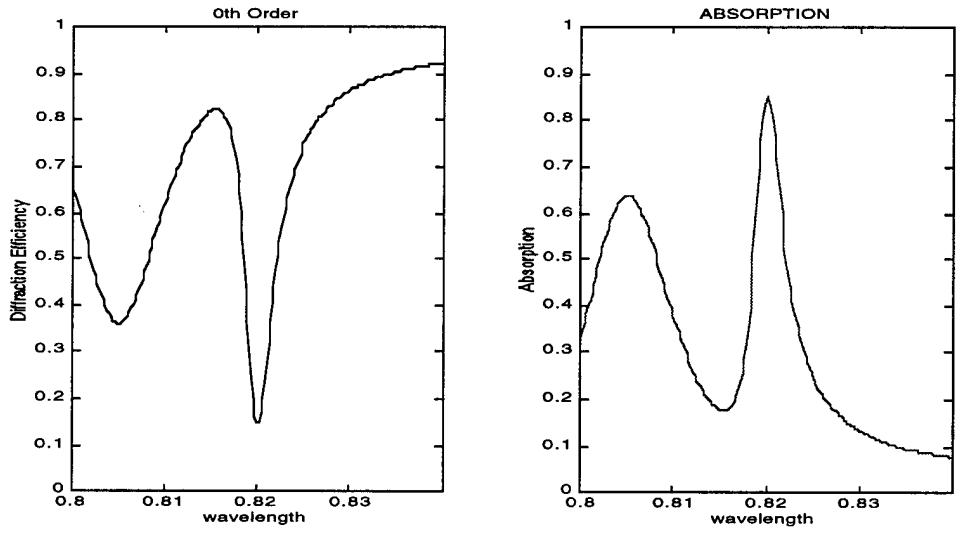

Figure 2E.13 - Optimized design for a λ = 820 nm resonance.
Thicknesses: 730 nm SiO_2, 460 nm Si, 97 nm Au, and 194 nm α-Si
Λ = 735.5 nm, R_{MIN} = 0.1482, R_{MAX} = 0.9233, LW = 3.8 nm

Chapter 3 Experimental Description

3.1 Fabrication Process

Optimized designs were built on several readily available silicon on insulator (SOI) wafers. Three distinct pre-fabricated waveguides were available for this research. Two of these SOI structures were fabricated using the bond-and-etchback process[17] and the third by growth of polycrystalline silicon using plasma-enhanced chemical vapor deposition. The SiO_2 was thermally grown. Table 3.1 contains the characteristics of these wafers.

	Layer Thickness		Fabrication
Wafer ID	**Si (μm)**	**SiO_2 (μm)**	**Method**
A	0.550	0.534 ± .030	PECVD (poly-Si)
B	1.04	2.30	BESOI (c-Si)
C1	0.730 ± .001	0.459 ± .011	BESOI (c-Si)
C2	0.728 ± .001	0.439 ± .019	BESOI (c-Si)

Table 3.1 - Characteristics of available SOI wafers

In order to experimentally test the optical properties of the optimized models in a timely manner, it was necessary to develop an in-house fabrication process. The fabrication of these structures consisted of four-steps: depositing the metal film, recording a holographic grating in photoresist, transferring the grating into the metal film, and depositing an α-Si overcoat.

Deposition of gold was conducted using the Denton III cold sputter/etch system. Operated in the sputter mode, this unit deposits a uniform gold film on the surface of the samples. Argon is used as the inert gas, and the control panel enables manual

manipulation of the gas pressure and electrical current. Prior to use, the deposition rate for gold was calibrated to be either 25 nm/min or 15 nm/min, depending on the source used. (The initial foil targets eventually started to show signs of wear from excess bombardment and were replaced by a thicker plate target.)

Gratings were produced using wave-front division holography.[20] Interferometric exposures were conducted using a Lloyd's mirror arrangement and the 458 nm line of an argon laser. With this method, the collimated beam is centered on the corner created by the mirror and the UV sensitive sample as shown in figure 3.1.

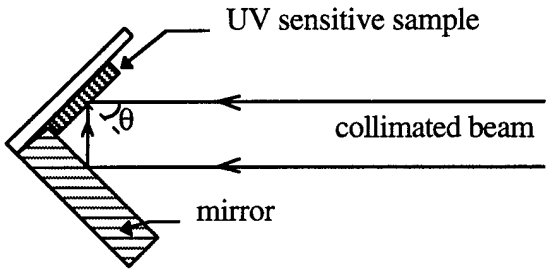

Figure 3.1 - Geometry of Lloyd's mirror arrangement

The desired grating period (Λ) is easily achieved by simply rotating the entire Lloyd's mirror arrangement which changes the angle of the incident beam (θ):

$$\theta = \sin^{-1}\left(\frac{\lambda}{2\Lambda}\right). \tag{3.1}$$

Once recorded, the resist serves as the template for transferring the grating to the metal film. Utilizing a positive photoresist (Shipley 1805), exposed regions are removed upon developing and produce a periodic grating on the sample.

The most difficult step in the fabrication process is the reliable transfer of the pattern into the metal. We used chemically-assisted ion-beam etching (CAIBE) with some degree of success to etch our gold film. The CAIBE method, as its name implies, uses

a reactive gas to introduce a degree of selectivity to the otherwise poorly selective ion milling technique. The ion milling portion of the system is achieved when the ions from a nonreactive plasma are accelerated and bombard the sample with sufficient momentum to remove surface atoms. Reactive gas is introduced to the system via a separate jet.

The CAIBE system uses argon (Ar) as the inert gas, and chlorine (Cl_2) as the reactive agent. The chamber of the system is evacuated during an etch by a diffusion pump that is aided by a liquid nitrogen cold trap. When not etching, the chamber is continually pumped via a separate cryopump. During ion beam adjustment, the target is protected by a rotary shutter, and a switch allows for manual control of reactive gas flow.

The use of a reactive chlorine-assist increases the etch selectivity - in our case the gold was found to etch roughly three times as fast as the resist. Chlorine-assisted ion beam etching is generally considered to be ineffective on silicon. We found, however, that the etch did not simply stop at the silicon surface but continued at a rate comparable to the etch rate of the gold. Therefore, the etch had to be carefully calibrated in order to minimize the removal of material from the silicon waveguide. Taking advantage of the system's tiltable stage, we introduce a 20° etch angle and orient the sample on the stage so that sputtered material is forced away and prevented from redepositing (see figure 3.2).

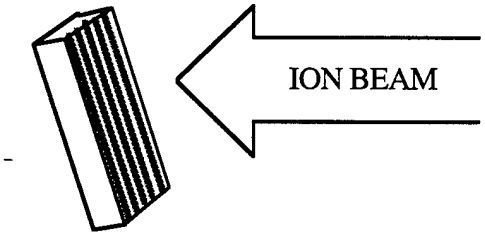

Figure 3.2 - Orientation of sample in ion beam

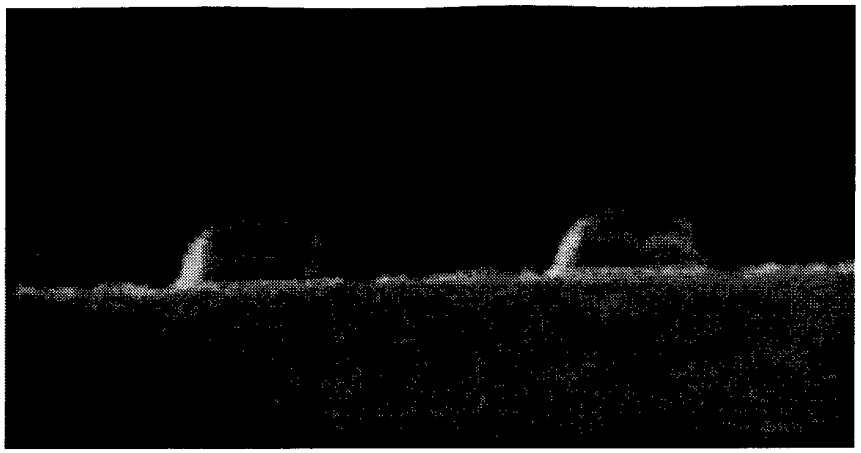

Figure 3.3 - SEM micrograph of sample following the chlorine-assisted etch

Figure 3.3 shows the fabrication results immediately following chlorine-assisted etching. The profile clearly shows the production of a somewhat trapezoidal gold grating (Λ=610), with a duty cycle of approximately 40%. Additionally, we can see the unetched resist remaining as a cap on the gold finger. Once etched, the final step in the process was to remove any remaining photoresist. This was accomplished by immersing the samples in resist stripper.

The overcoat was provided by electron beam evaporation of silicon. In this technique, a filament emits electrons that are then formed into a beam by a cathode assembly and accelerated through a steep potential gradient. A magnetic field then focuses the beam onto the source material. Upon striking the source, the electrons' kinetic energy produces sufficient thermal energy to melt a portion of the source material, and produces a vapor rising from the source surface. To allow for uniform evaporation, a programmable controller is used to continually sweep the beam over a large area of the source material. The chamber itself is kept under high vacuum by a diffusion pump and aided by a cold trap of liquid nitrogen.

For the amorphous silicon evaporations performed for this work, a graphite crucible was used. The electron beam was swept in a figure-8 pattern of amplitude 3.5 (max of 5.0) and with an acceleration voltage of 9.3 kV. The deposition was performed using a combination of the programmable and manual modes of the deposition rate controller. All depositions were conducted with a 3 minute ramp to a 3.0% soak for 2 minutes, followed by a second 3 minute ramp to a 5.0% soak for 2 minutes. Following the second soak, the power was manually increased to 7.5% and the shutter opened to begin deposition.

Appendix 3A details the fabrication process and includes partial operating instructions for some of the equipment used. A micrograph of a typical sample produced by this process is shown in figure 3.4.

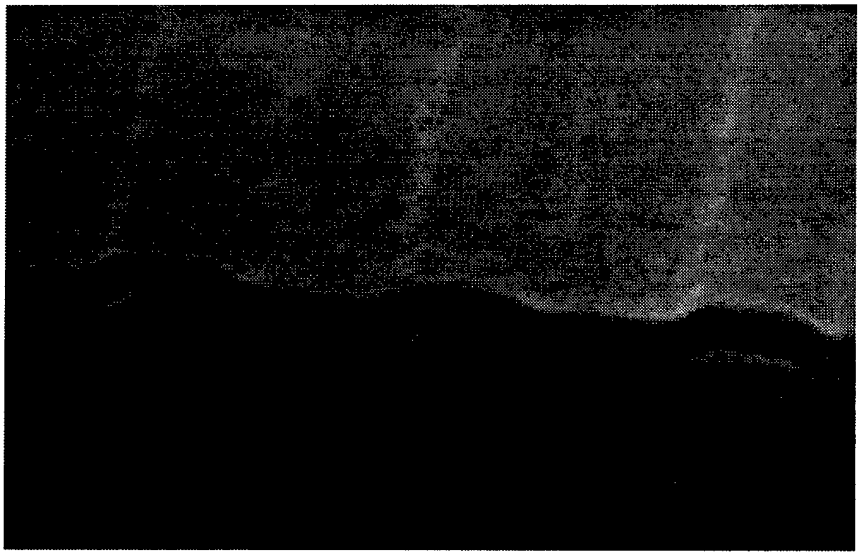

Figure 3.4 - Typical fabricated ORPEL structure
(Au: 50 nm, α-Si: 114 nm, Λ=783 nm)

3.2 Fabrication Results

The adhesion of the gold grating to the underlying silicon layer posed one of the key fabrication problems in this research. On numerous occasions, usually following either photoresist developing or rinsing, the gold film showed signs of peeling. In the most severe cases, samples were rendered useless. Preceding the gold deposition with a 10-20 second etch (under vacuum) appeared to alleviate the adhesion problem. (Argon ion beam etching removes surface contaminants and excess oxide.) Other possible improvements could include the introduction of a very thin titanium film prior to gold deposition[9], a very high temperate bake (annealing) immediately following deposition, and more sophisticated deposition methods.[21] However, the above procedure produced an ample supply of samples with uniform regions of up to 1 cm^2 in area.

Fabrication efforts focused on the seven optimized designs listed in table 3.2. The models selected for fabrication were dictated by the choice of SOI wafers on hand as well as the experimental set-ups readily available to conduct characterization. During the course of this work, 65 ORPEL structures were fabricated through completion. (Dozens more remain in various stages short of completion) A complete list of these structures (along with their associated parameters) appears in appendix 3B.

The successful fabrication of optimized designs is predicated by the use of accurate and consistent techniques. Any variation in layer thickness, duty cycle, grating shape, or refractive index from the optimized model will alter the characteristics of the resonance. The ORPEL structure's numerous degrees of freedom, require predictable fabrication methods. Any particular deviation from the model can just as easily drive the resulting structure away from the optimized design as it can compensate for prior fabrication errors.

wavelength	Wafer A	Wafer B	Wafer C
0.820 μm	67	46	97
	736	732	736
	166	94	194
1.064 μm	50	62	No Optimized
	783	748	Design Available
	100	125	
1.550 μm	70	89	114
	610	895	686
	231	178	197

Table 3.2 - Optimized parameters of fabricated structures
The set of three numbers at a given design represents the gold grating thickness (t_3), the grating period (Λ), and the amorphous silicon overcoat thickness (t_4+t_5) in nm.

As previously stated, the modeling of all gratings was done with the assumption that profiles are rectangular. However, following fabrication, metallic gratings assumed more of a trapezoidal profile as shown in figure 3.5, and the amorphous silicon overcoat followed the same contour. Rigorous results of the structure, now remodeled with this trapezoidal profile, can be compared to our original design. A typical trapezoidal profile ranges in duty-cycle from approximately 0.6 at the bottom surface to 0.3 at the top. Also visible in this micrograph is the structure's 125 nm α-Si undercoat. Figure 3.6 shows the effect trapezoidal gratings have on the waveguide resonance. It not only shifts the resonance away from the target wavelength, but reduces the contrast between maximum and minimum reflectance. While the grating period can be changed to "tune" the resonance back on target (as is done in all the designs) the loss of contrast is not automatically compensated. However, if the post-fabrication profile is consistent, then the structure can be optimized accordingly. More

sophisticated etch techniques could certainly produce a rectangular metallic grating but the conformal amorphous silicon coating would still produce angled sidewalls.

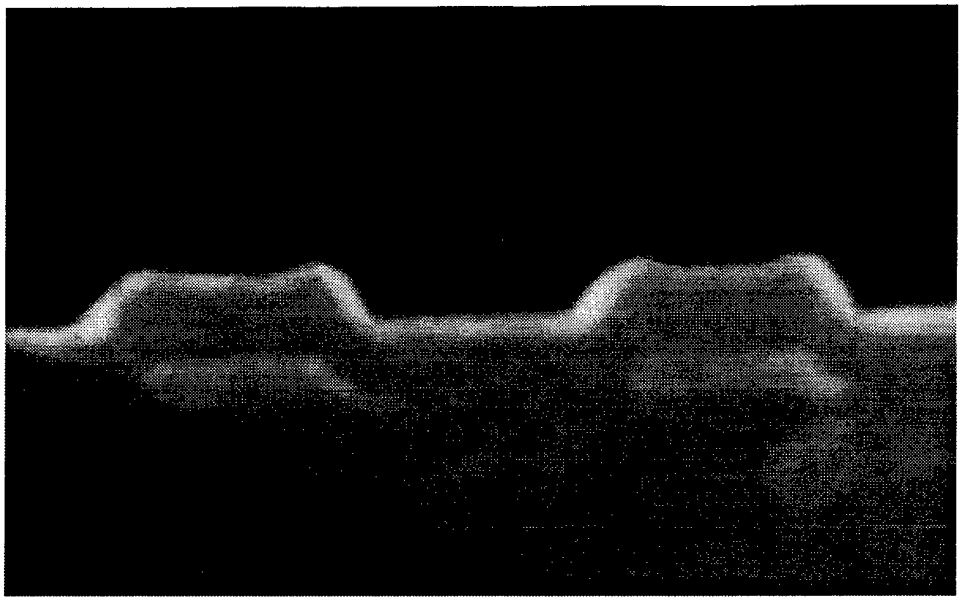

Figure 3.5 - Grating profile of a typical sample
Au = 46 nm, α-Si = 100 nm, Λ = 731 nm

All designs of the present study were modeled with a 50% duty cycle. Like the trapezoidal shape, this affects the quality of the resonance. An identical structure modeled with a duty cycle of 0.4, 0.5, and 0.6 is shown in figure 3.7. Altering the grating period allows the resonance to be brought on target, and the resonance's characteristics still appear close to optimum. Here, the 0.4 duty-cycle model (dashed line) has broadened only slightly and the 0.6 model (dotted), although losing some contrast, remains quite sharp.

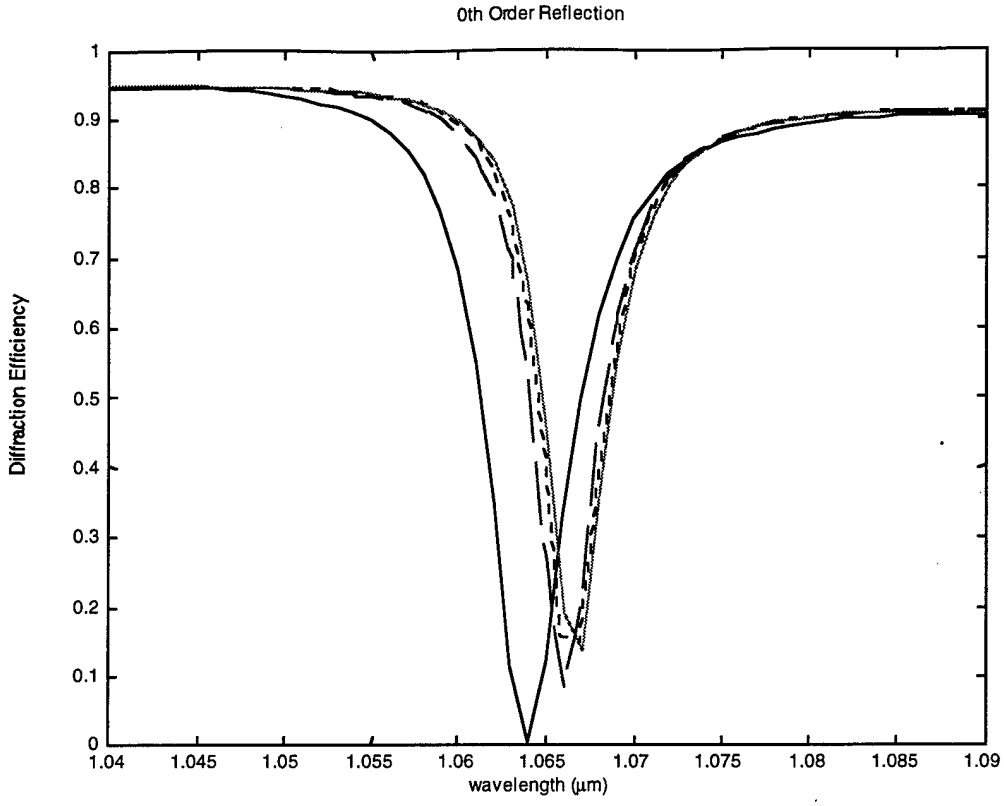

Figure 3.6 - Effects of trapezoidal grating profiles
The dashed, dotted, and solid resonances are the results of trapezoidal profiles modeled by 2, 4, and 8 rectangular sub-layers, respectively. For comparison, the deepest and left-most resonance is the result of a rectangular grating.

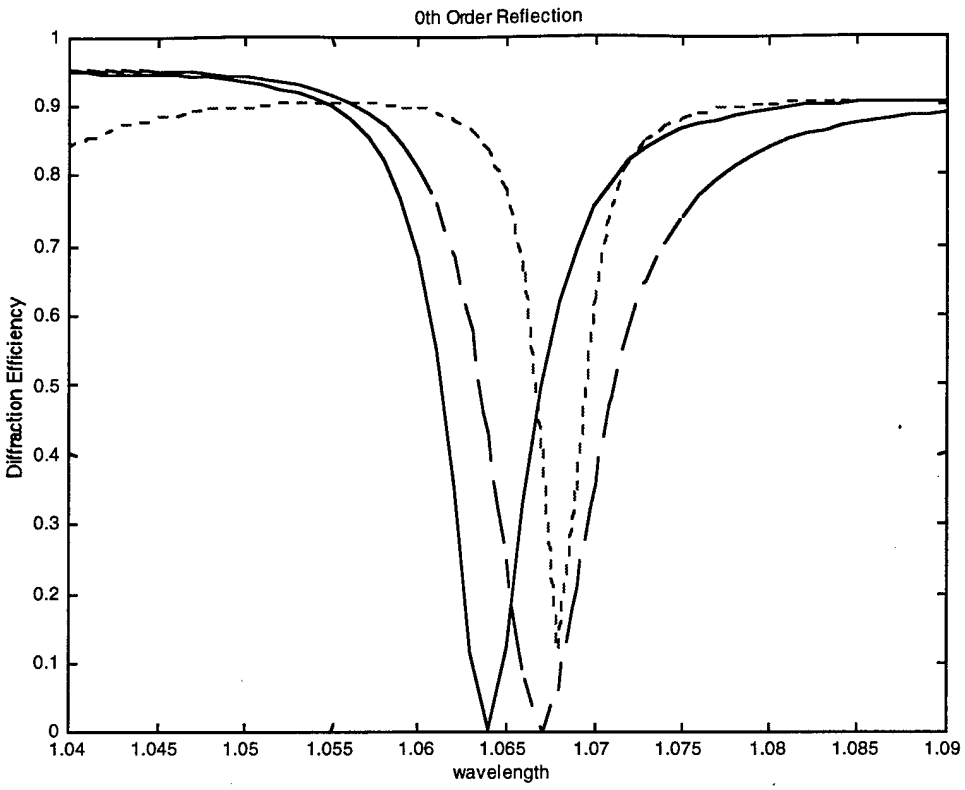

Figure 3.7 - Effects of duty-cycle variations
The dashed, solid, and dotted resonances are the results of profiles modeled with duty-cycles of 0.4, 0.5, and 0.6, respectively.

Surface roughness at any depth of our multilayer can cause resonance broadening through scattering. A major contributor to surface roughness in our process appears to be inadequate cleaning procedures. Any unwanted particles remaining on the SOI wafer are overcoated during the metal deposition. An insufficiently clean metal film creates additional nonuniformity during the spinning of photoresist. Contaminants, such as dust and water, can infect the structure at any step of fabrication.

Over-etching during fabrication poses two problems. First, if the etch continues beyond the bottom surface of the gold, the grating period will be transferred into the

waveguide layer of the SOI structure. Figure 3.8 shows an over-etched sample. In the case of 1550 nm designs this problem is somewhat alleviated by the fact that the amorphous silicon overcoat will fill the etched portion of the waveguide layer without altering its refractive index. Unfortunately, any α-Si deposited in this manner, will produce a departure from the overcoat thickness (t_4) of the optimized design. Second, over-etching of the resist would result in metallic grating thicknesses that are thinner than dictated by optimized designs. This likelihood is apparent in figure 3.8 since there appears to be no evidence of remaining resist on top of the gold fingers. Therefore, the resulting thickness of our gold grating is unknown.

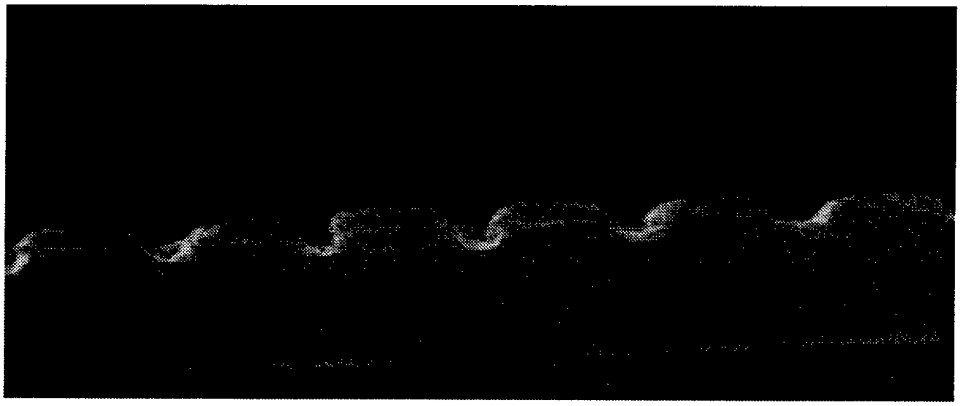

Figure 3.8 - Micrograph of over-etching into silicon waveguide

Deviation from an optimized model may also be caused by under-etching the gold film. This effectively introduces a thin metallic film into the interface between the grating and the waveguide layer. Again, more advanced fabrication techniques can alleviate this problem.

Reliable and predictable fabrication methods, such as photo- or electron-beam lithography will eliminate most of these variations. If duty-cycle and grating shape

variations can be better controlled, optimized designs may exist which depart from our assumption of half-period rectangular gratings. In regard to electronic fabrication and simplicity, square shapes will always be more desirable.

Due to a failure of the diffusion pump on the CAIBE system during the fabrication process, alternate etch methods were attempted that deserve brief comment. The first such method used was that of wet etching. A hydrochloric (HCl) and nitric acid (HNO_3) solution was found to etch through the gold film while leaving the photoresist intact. Unfortunately, this method, although promising at first, resulted in incomplete and inconsistent etching in the troughs of the grating, where the gold should have been removed (figure 3.9). The incomplete etching may be due to underexposed areas of the photoresist which, when developed, leave a nonuniform resist layer over the undesired gold regions. The second attempt to transfer the recorded grating into the gold film used ion milling. The same sputter/etch system used to deposit the gold film was used, but in the etch mode. This method failed, apparently, due to a tendency for the photoresist to oxidize (ash). We presume this was due to inadequate vacuum. After discovering that connecting the gold film to the sample stage with a conductive material (silver paint) enabled some degree of etching, the first of this work's gratings were produced. This method, while producing several satisfactory samples, proved inconsistent and was abandoned for the more reliable dry-etch process.

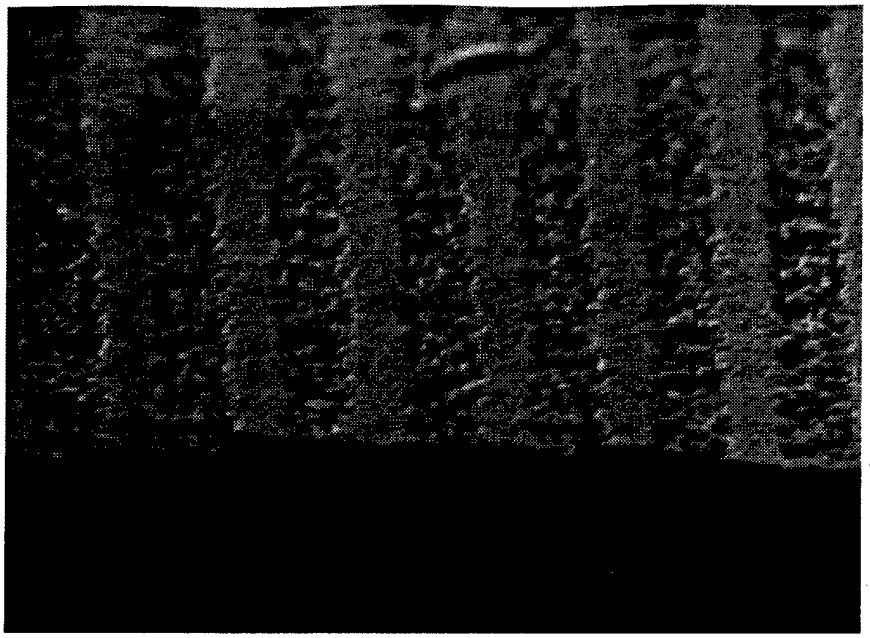

Figure 3.9 - Gold grating following wet-etch (HCl/HNO_3 solution)

3.3 Experimental Set-up

Two separate experimental set-ups were used to characterize fabricated structures. One was to measure the optical properties of the $\lambda = 1.064$ μm (Nd:YAG laser) designs and another to evaluate the $\lambda = 1.550$ μm models. The experimental results obtained with these two set-ups is contained in the following chapter. Ideally, a third system, capable of characterizing the $\lambda = 820$ nm designs, would have provided results for three more classes of fabricated structures. Unfortunately, due to time and resource constraints, such characterization was not possible, and will have to remain as future work.

Mounted on a dual-rotation stage, the first set-up (figure 3.10) allows the sample to rotate through a range of incident angles. The reflectance is measured and collected by an integrating detector connected to data acquisition software. In this system, the precise alignment of the sample's center of rotation with the incident beam (provided by

a Nd:YAG laser operating at 1.064 μm) is critical, as any beam walk-off creates experimental error. This set-up was originally configured by Dr. Amy Bieber to study reflectivity of input and output couplers.[9-11]

The second set-up allows characterization of optimized resonances designed for the 1550 nm regime. In this configuration (figure 3.11), the same single mode fiber is used to direct the incident beam as well as retrieve the reflected beam. Unlike the configuration of the 1.064 μm set-up, this allows the wavelength to be varied while measuring the sample's normal incident, 0^{th} order reflectance. Data produced by this means is directly comparable to theoretical results presented so far.

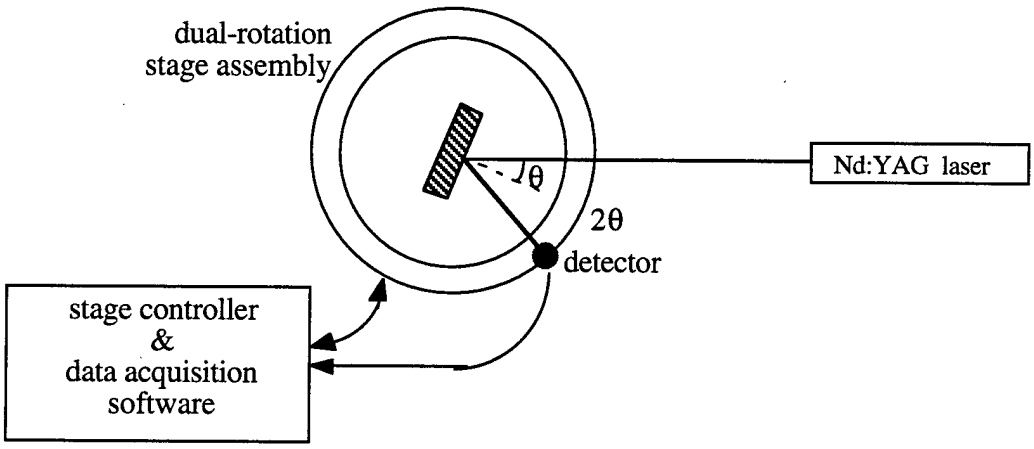

Figure 3.10 - Experimental set-up for 1.064 μm characterization

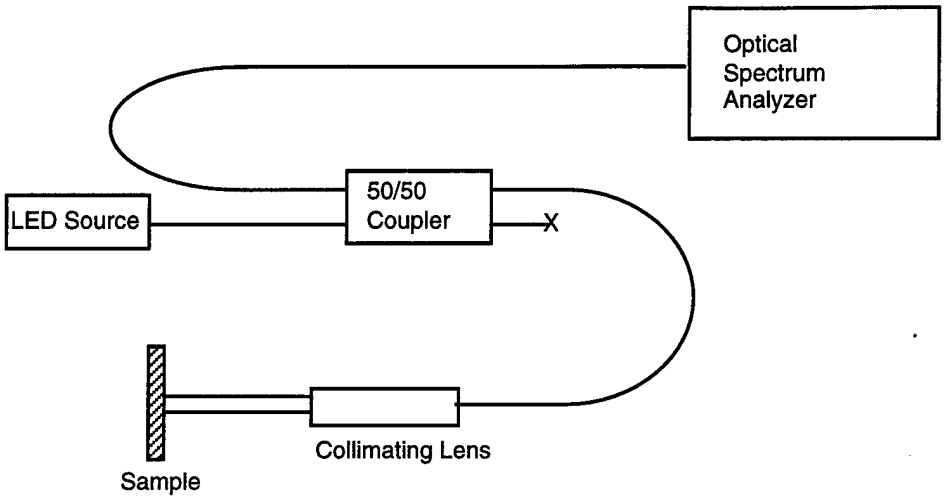

Figure 3.11 - Experimental set-up for 1550 nm characterization

Appendix 3A Fabrication Procedures

Cleaning

1. Soak cleaved SOI samples in a heated (hot plate on LOW) acetone bath for 20 minutes.
2. Rinse samples in deionized water for 5 minutes.
3. Blow dry with compressed nitrogen (N_2).
4. Immerse samples in isopropyl alcohol for 5 minutes.
5. Dry with N_2.

Gold Deposition

Procedures for sputter/etch system in SEM lab

1. Open compressed argon (Ar) cylinder.
2. Open chamber and ensure gold target is in place.
3. Load samples onto stage.
4. Close chamber.
5. Turn on system. (Power switch is located on right side of unit)
6. Place system into etch mode by selecting the "ETCH" button.
7. Allow chamber to evacuate by cycling pressure from below 50 mT to greater than 200 mT, twice.
8. Set chamber pressure to 50 mT.
9. Etch sample for 10 seconds at the maximum current - approximately 20 mA. (This step cleans the sample of any contaminates)
10. Switch system to sputter mode by selecting the "SPUTTER" button.
11. Allow chamber pressure to stabilize to 50 mT.

12. Enter sputter time into pre-set dials.

    NOTE: The gold target currently on hand sputters at 15 nm per minute (at 50 mT and 40 mA). This calibration is based on two back-to-back 60 second depositions, so it is advisable to deposit in near 60-second increments. (Example: For a 70 nm gold film, perform five 56-second depositions instead of one 280-second deposition)

13. Pre-adjust current for approximately 40 mA by aligning marks on knob and panel. (The current will not be displayed until the deposition process is initiated)

14. Start deposition by pressing "START" on the timer panel. (The sputter will cease when it reaches zero)

15. Monitor both gauges and readjust to maintain 40 mA and 50 mT.

16. After deposition is complete, press the "OFF" button and turn power switch off. (The chamber will leak back to atmosphere, and samples may be removed)

17. When all gold films have been deposited, close Ar bottle.

Photoresist Spinning

1. Prior to entering clean room, open N_2 bottle and adjust regulator to 28-30 psi.
2. Once in the clean room, turn pump on. (The pump for the system is located on the floor to the right of the unit)
3. Turn spinner controller on.
4. Place first sample on the chuck.
5. Start system by pressing foot control.

    NOTE: At this time, you should adjust the duration and speed of the spin. For an 80 nm film, spin 1:2 (1805:P-type thinner) photoresist solution at 4.5K RPM for 60 seconds.

6. Once satisfied that the spin time and rate are appropriate, spin the sample and blow with N_2.
7. Drop photoresist from clean pipette onto stationary sample. (Allow photoresist to bead at sample's edge)

8. Spin sample.
9. Soft-bake samples on 115° hot plate for 60 seconds. (Using silicon "baking" wafers between the hot plate surface and samples prevents samples from sticking)

NOTE: The samples are now sensitive to UV light, so take precautions to avoid accidental exposure.

Holographic Exposure

Procedures for Interferometric recording with argon laser

1. Turn on cooling water.
2. Turn on laser (both key and "ON" button).
3. Float table at 55 psi.
4. Ensure holographic grating set-up is properly configured and aligned.

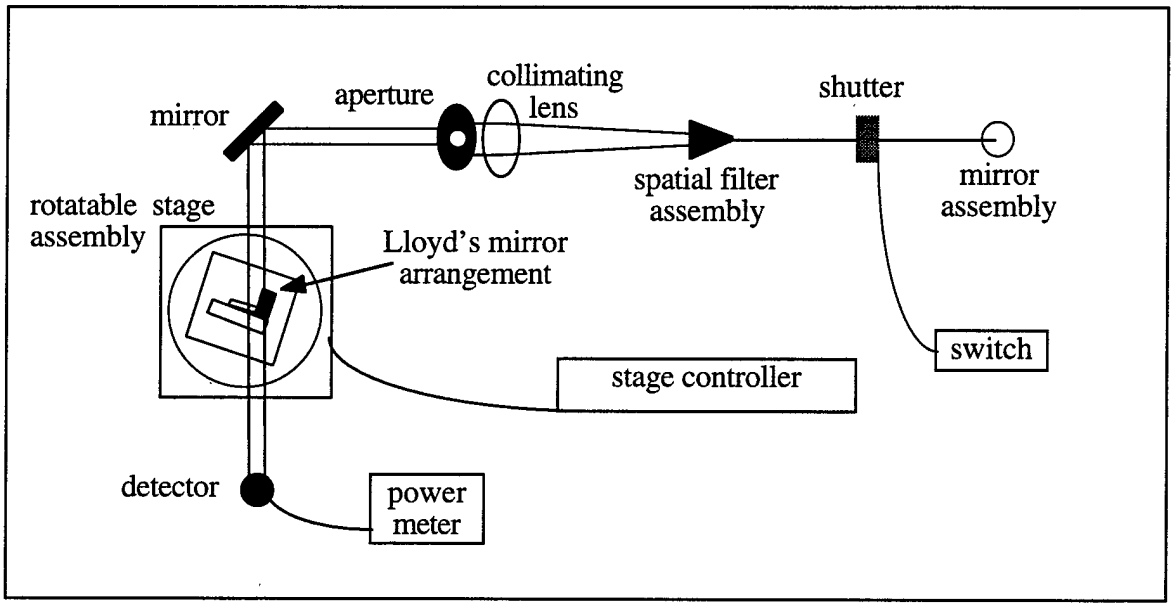

5. Adjust power meter to detect wavelength of 460 nm.
6. Set stage at normal incidence by retroreflecting beam back to pinhole or stopped down aperture and zero stage controller.

7. Set laser to desired output power.

   NOTE: For a 80 nm photoresist film, a 13 sec. expose at 9 mW works well.

8. Rotate stage to desired angle.

$$\theta = \sin^{-1}\left(\frac{\lambda}{2\Lambda}\right)$$

9. Close shutter.

10. Mount sample to microscope slide, slide to Lloyd's mirror arrangement, and mirror arrangement onto rotating stage.

11. Set desired shutter time.

12. Expose sample by opening shutter.

    NOTE: Prior to recording, ensure all vibrations are minimized by turning off stage controller and air vent.

13. Remove sample.

Developing

1. Prior to entering clean room, open N_2 bottle and adjust regulator to 25 psi.

2. Develop in Shipley 452 for 45 seconds.

   NOTE: Suspending and manually agitating sample held in tweezers in a 25 mL beaker of developer worked well.

3. Rinse in deionized water.

4. Dry with N_2.

   NOTE: Refresh developer and water as necessary.

5. Bake samples in 130° oven for 30 minutes and allow to cool slowly.

Etching

Procedures for CAIBE

1. Vent loadlock.
   - Loosen door.
   - Open vent bottle (N_2).
   - Turn LOADLOCK dial to "VENT".
   - Close N_2 when pressure reaches 7.5 x 10^2 T.
2. Mount samples.

   NOTE: Use gloves and keep loadlock door closed at all times to prevent chamber contamination.
3. Pump loadlock.
   - Turn LOADLOCK dial to "ROUGH".
   - When pressure reaches 1.5 x 10^{-2} T, turn LOADLOCK dial to "PUMP".
4. Allow loadlock to pump down to 10^{-6} T range. (This will take at least six hours)
5. Pump out Cl_2 line.
   - Note chamber pressure.
   - Switch JET to "ON".
   - Turn MFC's channel 2 "ON".
   - Allow chamber pressure to return to baseline.

     NOTE: This is a good time to fill the cold trap - step 7.
   - Turn MFC flow "OFF".
   - Switch JET to "OFF".
6. Load sample.
   - Record loadlock pressure in logbook.
   - Turn on degassing bulb.
   - Turn LOADLOCK dial to "OPEN GATE".

- Transfer sample onto sample stage.

  NOTE: Ensure transfer rod is pulled back prior to closing gate valve.

- Turn LOADLOCK dial back to "PUMP".

- Pivot stage to desired etch angle.

- Turn off degassing bulb.

7. Fill cold trap with liquid nitrogen (LN).

8. Open PROCESS OUT valve in Cl_2 cabinet.

9. Turn MODE dial to "ETCH".

   NOTE: Ensure that the pressure regulator in the Cl_2 cabinet is indicating at least 25 psi. If not, leak Cl_2 into the system by opening the Cl_2 bottle until the pressure increases, then, close the Cl_2 bottle.

10. Zero MFC's channels 2 (Ar) and 3 (Cl_2).

11. Set MFC's flow rates for channels 2 (2.0 sccm) and 3 (≈2.0 sccm).

12. Record chamber pressure in log book.

13. Start argon flow.

    - Open Ar bottle.

    - Open green Ar valve.

    - Switch MFC's channel 2 to "ON".

    - Ensure chamber pressure is at least 10^{-4} T. (If not, increase Ar flow)

14. Set up ion gun.

    - Turn magnet power supply "ON".

    - Ensure all knobs on ion beam source supply are fully counterclockwise.

    - Turn ion beam source supply "ON".

    - Press up on SOURCE switch.

    - Turn CATHODE knob two turns clockwise.

    - Set discharge voltage (55 V).

- Decrease discharge current to 0.3 A.
- Press up on BEAM switch.
- Set beam voltage (100 V).
- Set suppresser voltage (300 V).
- Reset beam voltage (400 V).
- Set beam current (25 mA) with CATHODE knob.
- Zero shutter current with NEUTRALIZER knob.
- Record setting in the log book.

NOTE: The settings in parentheses are those used during this fabrication

15. Etch sample.
    - Open Cl_2 isolation valve.
    - Set timer to desired etch time.
    - Switch MFC's channel 3 to "ON".
    - Loosen set screw on shutter but continue to hold shutter in place.
    - Start timer.
    - Simultaneously open the shutter and switch the JET to "ON".
    - Continually zero target current with NEUTRALIZER knob.
    - Maintain beam current (25 mA) with CATHODE knob.
    - Record process pressure in log book.
    - When etch time is complete, simultaneously close the shutter and switch the JET to "OFF".
    - Switch MFC's channel 3 to "OFF".
    - Close Cl_2 isolation valve.
16. Shut down ion gun.
    - Press down on both SOURCE and BEAM switches.

- Ensure all knobs on ion beam source supply are fully counterclockwise.
- Switch ion beam source supply to "OFF".
- Switch magnet power supply to "OFF".

17. Stop argon flow.
    - Switch MFC's channel 2 to "OFF".
    - Close green Ar valve.
    - Close Ar bottle.
18. Allow chamber to return to mid 10^{-7} T range.
19. Close PROCESS OUT valve in Cl_2 cabinet.
20. Retrieve sample.
    - Turn LOADLOCK dial to "OPEN GATE".
    - Turn on degassing bulb.
    - Transfer sample to loadlock.
    - Return LOADLOCK dial to "PUMP".
    - Turn off degassing bulb.
21. Pump out Cl_2 line.
    - Note chamber pressure.
    - Switch JET to "ON".
    - Turn MFC's channel 2 "ON".
    - Allow chamber pressure to return to baseline. (This may take up to 30 minutes)

      NOTE: This is a good time to vent loadlock and unload samples - steps 23-24.

    - Switch MFC flow to "OFF".
    - Switch JET to "OFF".
22. Vent loadlock.
    - Loosen door.

- Open vent bottle (N_2).

- Turn LOADLOCK dial to "VENT".

- Close N_2 when pressure reaches 7.5 x 10^2 T.

23. Remove samples.

    NOTE: Use gloves and keep loadlock door closed at all times to prevent chamber contamination.

24. Once step 22 is completed, turn MODE dial to "ETCH".

Overcoat Deposition

Procedures for electron-beam evaporation

1. Vent chamber.

    - Open N_2 bottle.

    - Open AIR INLET valve.

    - When chamber reaches atmosphere, close AIR INLET valve.

    - Raise bell jar.

    - Close N_2 bottle.

2. Load samples.

3. If necessary, fill silicon crucible so that it is 3/4 full.

4. Place silicon crucible in chamber.

5. Vacuum inside of chamber free of debris.

6. Replace inner shield.

7. Pump down chamber.

    - Lower bell jar. (Be careful not to scratch the edge of rubber gasket on shield)

    - Close FORELINE valve.

    NOTE: While FORELINE valve is closed, continually monitor foreline pressure. If it rises above .05, close ROUGHING valve and reopen FORELINE valve until pressure drops.

- Open ROUGHING valve.

NOTE: The roughing out of the chamber will take a while, so this is a good time to fill the liquid nitrogen trap - step 8.

- When chamber pressure drops below .05, close ROUGHING valve.

- Open FORELINE valve.

8. Fill liquid nitrogen trap.

9. Slowly open GATE valve. (Keep foreline pressure below .05)

NOTE: Whenever the diffusion pump is open to the chamber, ensure the LN trap stays frosted over.

10. Allow chamber to pump down for at least 4 hours.

11. Set up electron beam.

- Turn on deposition rate controller.

- Turn on sweep controller. (Power switch is on the back of the unit)

- Set sweep pattern. (typically: Figure 8, Amp 3.5, $1/R^2$, and Fast)

- Turn on current control.

- Switch power source circuit breaker to "ON".

- Press "HV ON" button.

- Turn voltage up to 9.30 kV.

- Press "FIL ON" button.

12. Start evaporation by pressing "START" and "4".

13. Prior to the end of soak-2, switch to manual mode.

14. With hand held controller, manually increase power to desired level. (7.5%)

15. Switch SHUTTER to "OPEN".

16. Press "RESET" to zero thickness.

17. When desired thickness is reached, switch SHUTTER to "CLOSE" and press "STOP".

18. Shut down electron beam.
    - Press "FIL OFF".
    - Press "HV RESET".
    - Turn VOLTAGE knob completely counter-clockwise.
    - Switch power source circuit breaker to "OFF".
    - Turn off current control.
    - Turn off sweep controller.
    - Turn off deposition rate controller.
19. Allow chamber to cool for 30 minutes.
20. Record setting in log book.
21. Close GATE valve.
22. Vent chamber.
    - Open N_2 bottle.
    - Open AIR INLET valve.
    - When chamber reaches atmosphere, close AIR INLET valve.
    - Raise bell jar.
    - Close N_2 bottle.
23. Ground high voltage leads with grounding rod.
24. Remove samples.
25. Vacuum inside of chamber and inside walls of shield.
26. If done for the day, evacuate chamber.
    - Close FORELINE valve.
    - Open ROUGHING valve.
    - When chamber pressure drops below atmosphere, close ROUGHING valve.
    - Open FORELINE valve.

Appendix 3B Fabricated ORPEL Structures

Wafer A Structures

Sample	SOI	λ	Thickness (nm)				Λ
ID	wafer	(nm)	SiO_2	Si	Au	α–Si overcoat	(nm)
sa501	A	1550	55	55	70	225.0	610
sa502	A	1550	55	55	70	225.0	610
sa503	A	1550	55	55	70	225.0	610
sa504	A	1550	55	55	70	232.0	610
sa601	A	1064	55	55	50	101.0	775
sa602	A	1064	55	55	50	202.0	775
sa603	A	1064	55	55	50	101.0	775
sa604	A	1064	55	55	50	107.0	783
sa605	A	1064	55	55	50	114.0	783
sa606	A	1064	55	55	50	114.0	783
sa607	A	1064	55	55	50	114.0	783
sa608	A	1064	55	55	50	114.0	783
sa609	A	1064	55	55	50	119.0	783
sa610	A	1064	55	55	50	96.0	775
sa611	A	1064	55	55	50	96.0	775
sa612	A	1064	55	55	50	96.0	783
sa613	A	1064	55	55	50	96.0	775
sa614	A	1064	55	55	70	96.0	783
sa615	A	1064	55	55	50	96.0	775
sa616	A	1064	55	55	50	105.0	775
sa617	A	1064	55	55	50	105.0	775
sa618	A	1064	55	55	50	105.0	775
sa619	A	1064	55	55	50	106.0	775
sa620	A	1064	55	55	50	106.0	783
sa621	A	1064	55	55	50	106.0	783

Wafer B Structures

Sample	SOI	λ	Thickness (nm)					Λ
ID	wafer	(nm)	SiO_2	Si	α–Si undercoat	Au	α–Si overcoat	(nm)
sb501	B	1550	103	230	145	89	205.0	895
sb502	B	1550	103	230	145	89	205.0	895
sb503	B	1550	103	230	145	89	170.0	895
sb504	B	1550	103	230	160	89	170.0	895
sb505	B	1550	103	230	145	90	181.0	894
sb506	B	1550	103	230	145	90	181.0	895
sb507	B	1550	103	230	145	90	181.0	895
sb601	B	1064	103	230	55	62	120.5	748
sb602	B	1064	103	230	55	62	120.5	749
sb603	B	1064	103	230	55	62	120.5	748
sb604	B	1064	103	230	55	62	120.5	749
sb801	B	820	103	230	125	46	100.0	733
sb802	B	820	103	230	125	46	100.0	731
sb803	B	820	103	230	125	46	100.0	731
sb804	B	820	103	230	125	46	100.0	733
sb805	B	820	103	230	96	46	100.0	732
sb806	B	820	103	230	96	46	100.0	732

Wafer C Structures

Sample	SOI	λ	Thickness (nm)					Λ
ID	wafer	(nm)	SiO_2	Si	α–Si undercoat	Au	α–Si overcoat	(nm)
sc501	C1	1550	73	46	16	114	180.0	686
sc502	C1	1550	73	46	16	114	202.0	686
sc503	C1	1550	73	46	16	114	180.0	686
sc504	C1	1550	73	46	16	114	180.0	685
sc505	C1	1550	73	46	16	114	202.0	685
sc506	C1	1550	73	46	16	114	194.0	686
sc507	C1	1550	73	46	16	114	194.0	687
sc508	C1	1550	73	46	16	114	194.0	687
sc509	C2	1550	73	44	37	114	197.0	686
sc510	C2	1550	73	44	37	114	197.0	685
sc511	C2	1550	73	44	37	114	197.0	687
sc512	C2	1550	73	44	37	114	197.0	686
sc513	C2	1550	73	44	37	114	197.0	686
sc514	C2	1550	73	44	37	114	197.0	687
sc801	C1	820	73	46		97	184.0	736
sc802	C1	820	73	46		97	184.0	736
sc803	C1	820	73	46		97	184.0	735
sc804	C1	820	73	46		97	184.0	736
sc805	C1	820	73	46		97	194.0	735
sc806	C1	820	73	46		97	194.0	736

Chapter 4 Results and Discussion

4.1 Optical Characterization of λ = 1550 nm designs

The following pairs of graphs compare the experimentally measured reflectance of fabricated structures with their corresponding theoretical models. In all cases, the theoretical model has been adjusted from the optimized design originally modeled. This was logical as actual α-Si overcoat thicknesses deposited during fabrication and grating periods were now known. However, no effort has been made to correct for fabrication related variations in duty-cycle, grating shape, or gold thickness. Accompanying each figure are the corresponding layer thicknesses and grating period, measured in nm, for that sample.

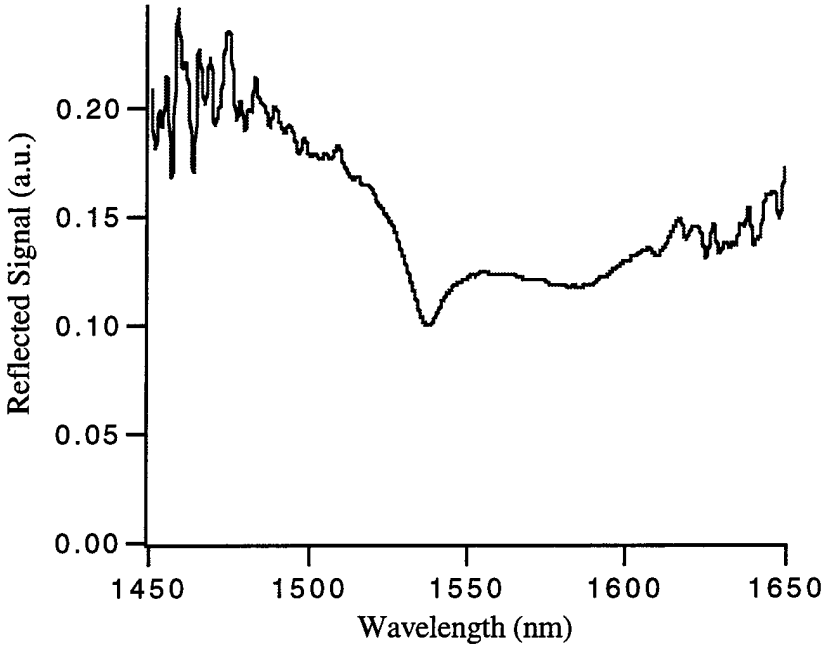

(a)

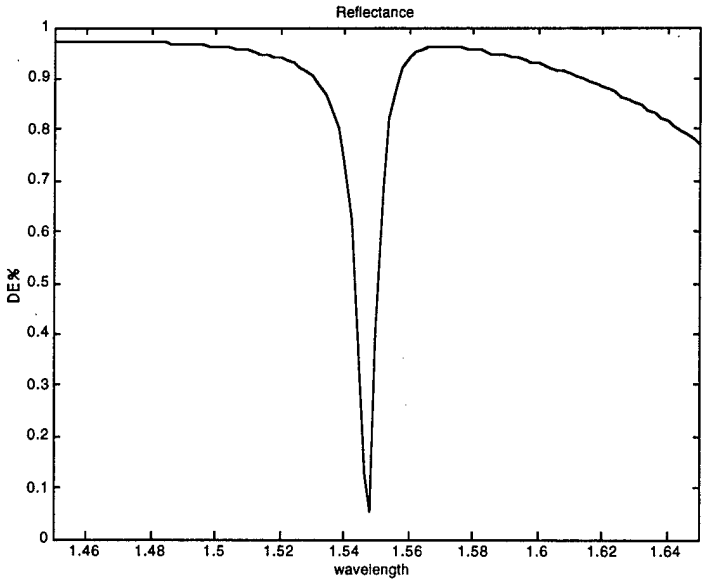

(b)

Figure 4.1 - (a) Experimental results and (b) theoretical model of structure (wafer A) (SiO_2: 530, Si: 550, Au: 70, α-Si: 225, Λ=610 nm)

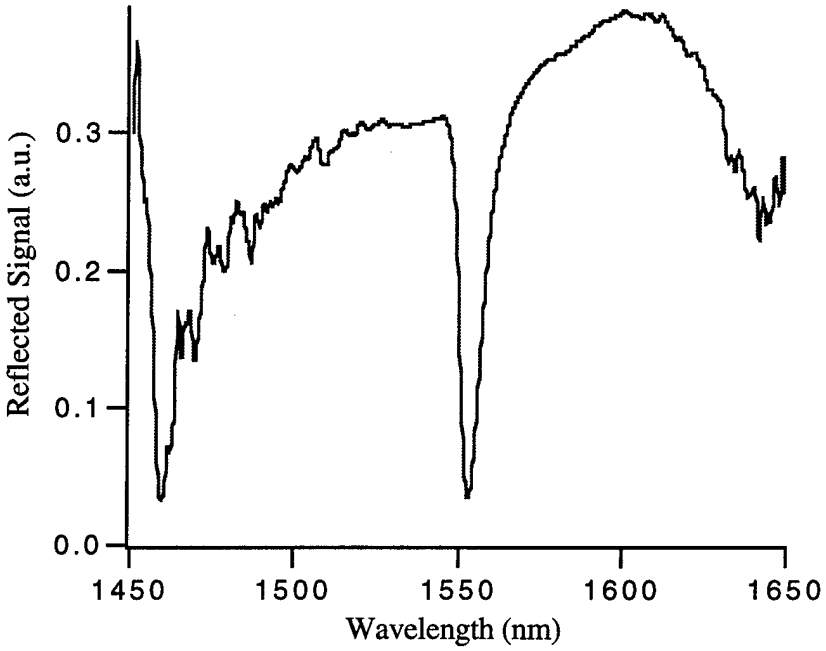

(a)

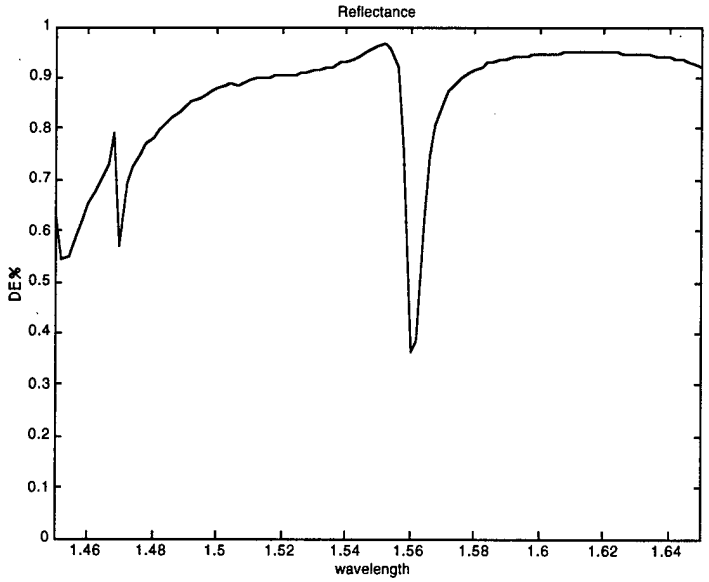

(b)

Figure 4.2 - (a) Experimental results and (b) theoretical model of structure (wafer B) (SiO_2: 1040, Si: 2300, α-Si: 145, Au: 89, α-Si: 205, Λ=895 nm)

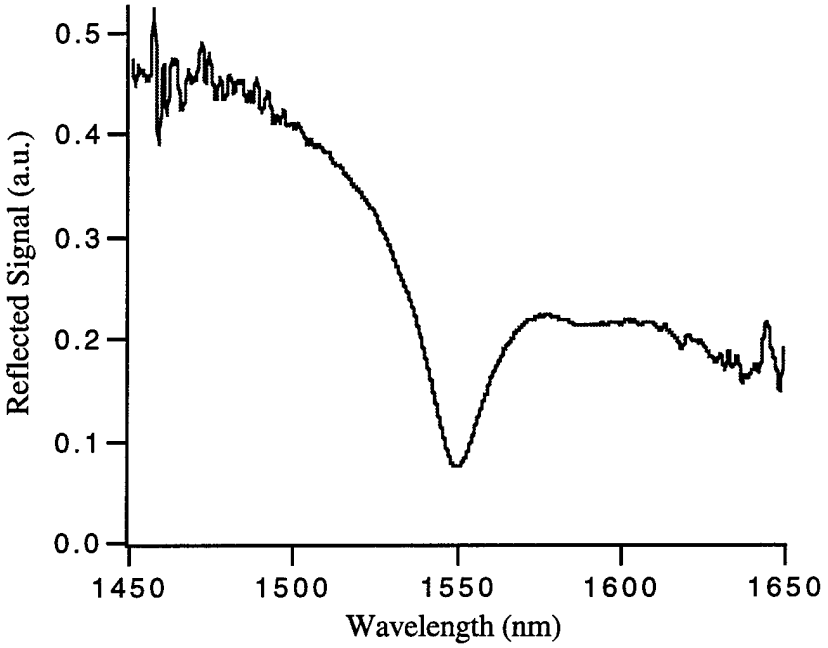

(a)

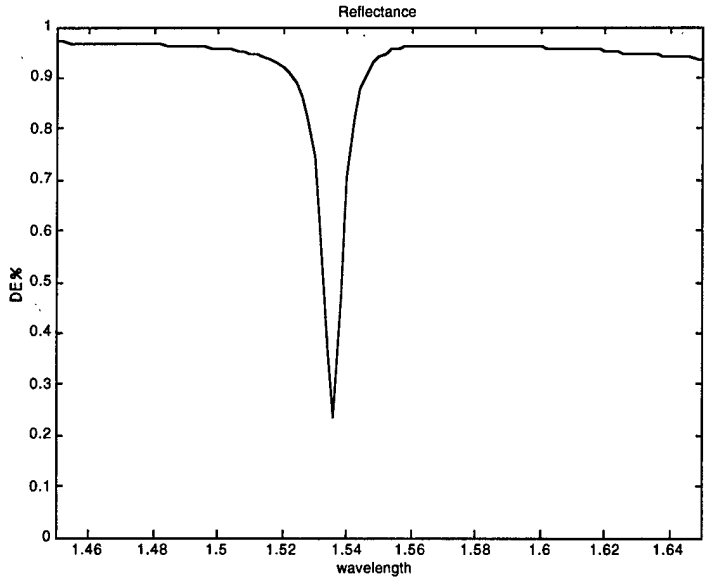

(b)

Figure 4.3 - (a) Experimental results and (b) theoretical model of structure (wafer C1) (SiO_2: 730, Si: 460, α-Si: 16, Au: 114, α-Si: 180, Λ=686 nm)

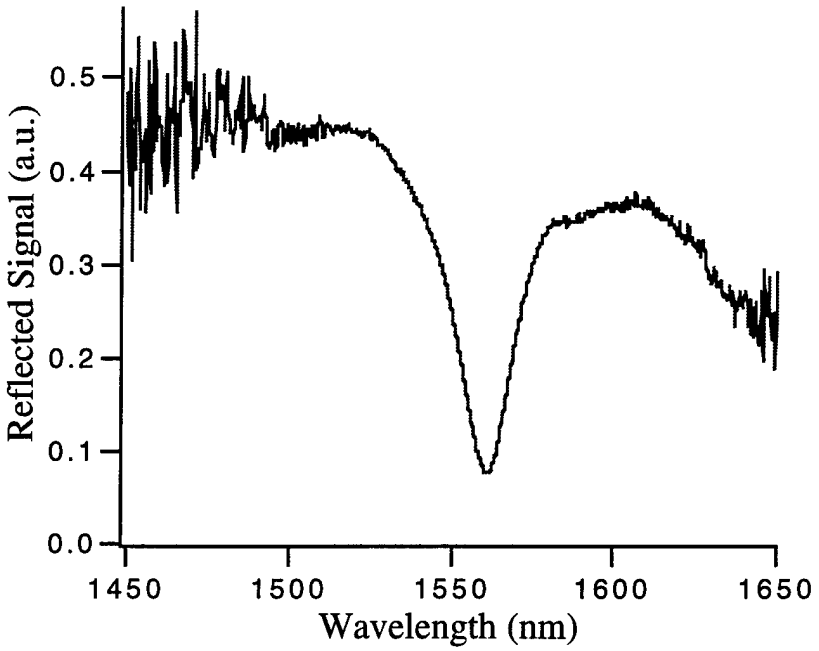

(a)

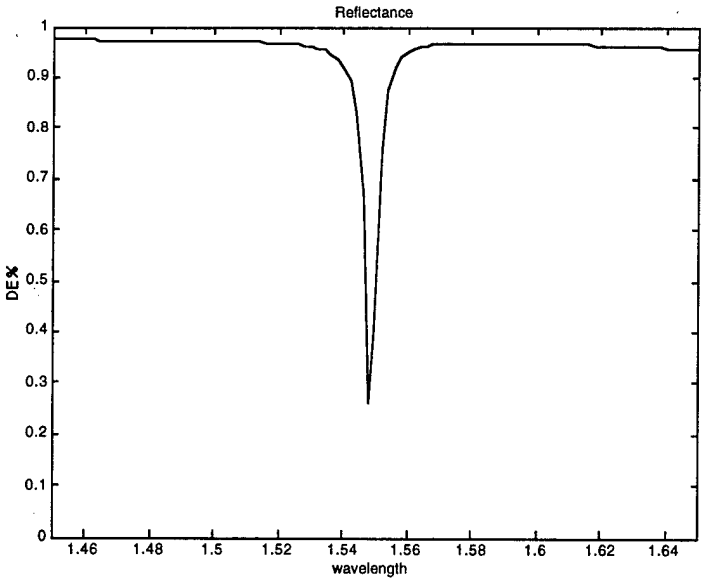

(b)

Figure 4.4 - (a) Experimental results and (b) theoretical model of structure (wafer C2) (SiO_2: 730, Si: 440, α-Si: 37, Au: 114, α-Si: 197, Λ=685 nm)

4.2 Optical Characterization of λ = 1064 nm designs

Unlike the resonance measurements for the λ = 1550 nm designs, the λ = 1064 nm set-up only permitted the angle of incidence to vary as it recorded reflectance measurements for a fixed wavelength. For this reason, the theoretical results shown here differ from those presented earlier. In these plots, the reflectance of the structure is calculated as a function of angle of incidence for a fixed wavelength. One disadvantage of this methodology is its inability to accurately determine the wavelength of the resonance. Since these models are now based on a fixed wavelength, any deviation in location of the resonance shifts the minimum reflectance found at normal incidence. Therefore, this method of characterization cannot reveal the depth sought through optimization. Similar to the previous section, the models used for comparison were calculated to account for known fabrication variations in layer thickness.

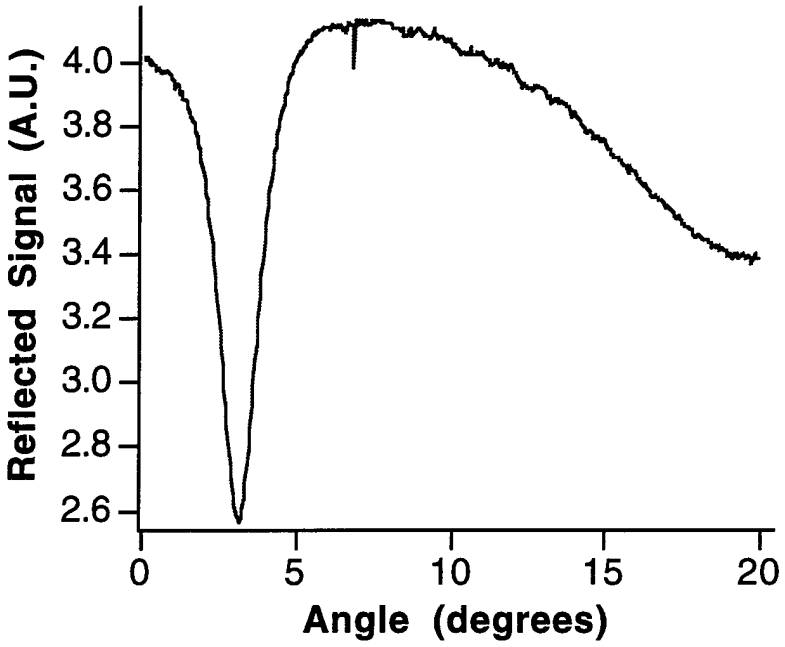

(a)

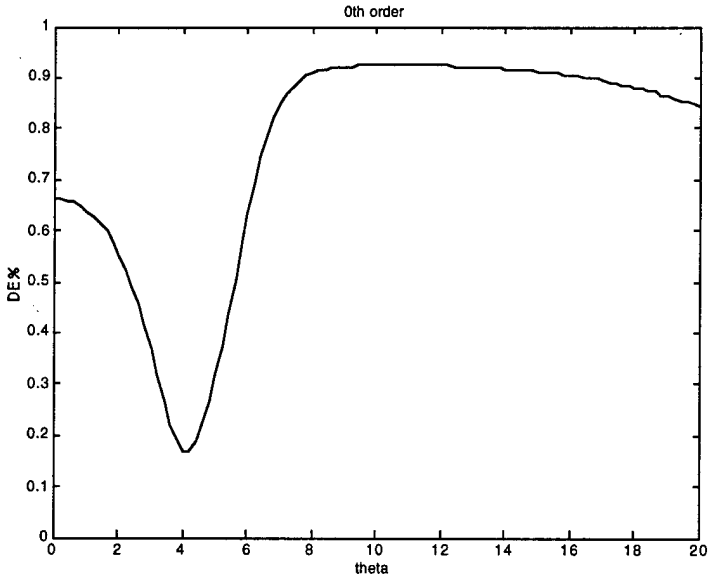

(b)

Figure 4.5 - (a) Experimental results and (b) theoretical model of structure (wafer A) (SiO_2: 530, Si: 550, Au: 50, α-Si: 107, Λ=783 nm)

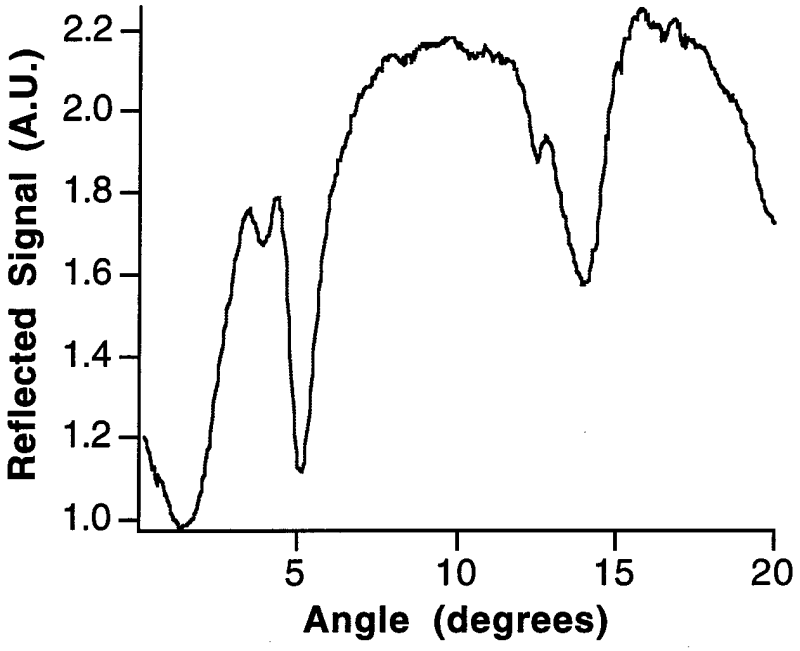

(a)

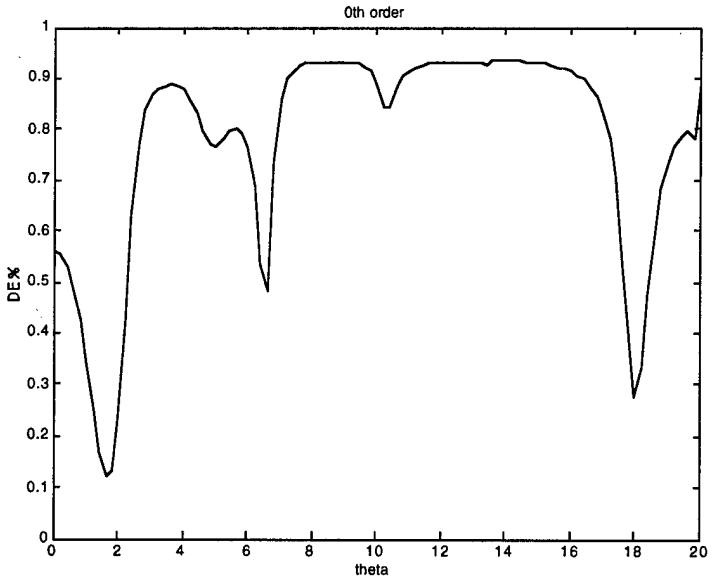

(b)

Figure 4.6 - (a) Experimental results and (b) theoretical model of structure (wafer B) (SiO_2: 1040, Si: 2300, α-Si: 55, Au: 62, α-Si: 120.5, Λ=748 nm)

4.3 Discussion

We can see that, in several cases, the experimental results at $\lambda = 1550$ nm closely match the rigorous results of the model. In the case shown in figure 4.1, the experimentally measured resonance was not nearly as deep or as sharp as we had expected. However, this model was built upon wafer A, the SOI structure with polycrystalline silicon as its waveguide. Much is still unknown in respect to the optical properties of poly-Si. We used the accepted c-Si refractive index (n=3.476) in this model, but know that poly-Si waveguides tend to have high scattering losses.

The data provided by the spectral scan of our second sample closely matches that predicted by its theoretical model (figure 4.2). Not only are the resonance's location, linewidth, and depth close to that of the model, but the structure's response below $\lambda =$ 1550 nm also shows consistency. The discrepancies between resonance wavelengths can easily be attributed to slight structure variations (grating thickness, shape, and duty-cycle) encountered during the fabrication process. Also encouraging in this particular model was the fact that an α-Si underlayer was deposited, beneath the gold, to increase the waveguide thickness to that of an optimized design. (Recall that at $\lambda = 1550$ nm, the refractive indices for c-Si and α-Si match to within three significant figures) This shows that a particular SOI structure can be used as the foundation for more than one optimized design, and therefore lessen the need for waveguides to be fabricated at different thicknesses.

For the experimental results of the $\lambda = 1.064$ μm structures, we again see a match with the theoretical predictions. For the poly-Si wafer (figure 4.5), theory predicts a resonance at an incident angle of approximately 4°, and experimentally we measure one at 3.2°. At normal incidence, we notice that the sample is close to its maximum reflectance. This is not surprising. As we can see from the theoretical model, we

expect the normal reflectance to be slightly off-resonance. Given the known thicknesses, the resonant wavelength in this particular sample would most likely be somewhere close to $\lambda = 1.069$ μm and have a minimum reflectance of around 3%.

For the thicker SOI wafer (figure 4.6), we again see many similarities between theory and experiment. As predicted by the model's rigorous results, resonances are evident at three locations: 1.5°, 5°, and 14°. Here, the normal reflectance appears much closer to be on-resonance than in the previous sample.

Many of the deviations between the results provided by theoretical modeling and those measured during experimental characterization may be directly attributed to inconsistencies in the fabrication process. We know from numerous optimization runs that it only takes a slight deviation in a layer of the structure to change the characteristics of the resonance. In addition to uncertainty in gold and α-Si thicknesses deposited during fabrication, the SOI waveguides used contain a fair amount of uncertainty - their insulator layers may vary as much as 2% to 6% in thickness (see table 3.1). This, combined with surface roughness and deviations from rectangular, half-period grating profiles limits full characterization of ORPEL structures until more advanced fabrication techniques are developed.

Overall, the experimental results of this work are very promising. The additional characterization of structures modeled and fabricated for the $\lambda = 820$ nm regime, should reveal even more about the potential capacity to optimize such structures. This short wavelength case is of special interest as it is the only one, of the three wavelength regimes modeled, that includes a complex refractive index for silicon ($k = 0.004$).

During routine SEM examination of a post-fabrication sample, an interesting observation was made. The profile of the amorphous silicon on the sample shown in

figure 4.7 revealed what seems to be two distinct morphologies. The α-Si that evaporated onto the gold fingers took on a round profile (indicating an amorphous or fine-grain poly-silicon structure), while that deposited on the silicon remained quite flat (indicating some mechanism of crystal growth). Additionally, there is a very distinguishable profile pattern created at the sample's edge. Apart from arousing curiosity about the mechanism at work, it re-emphasizes the importance of process control in achieving the very tight tolerances required of optimized ORPEL structures.

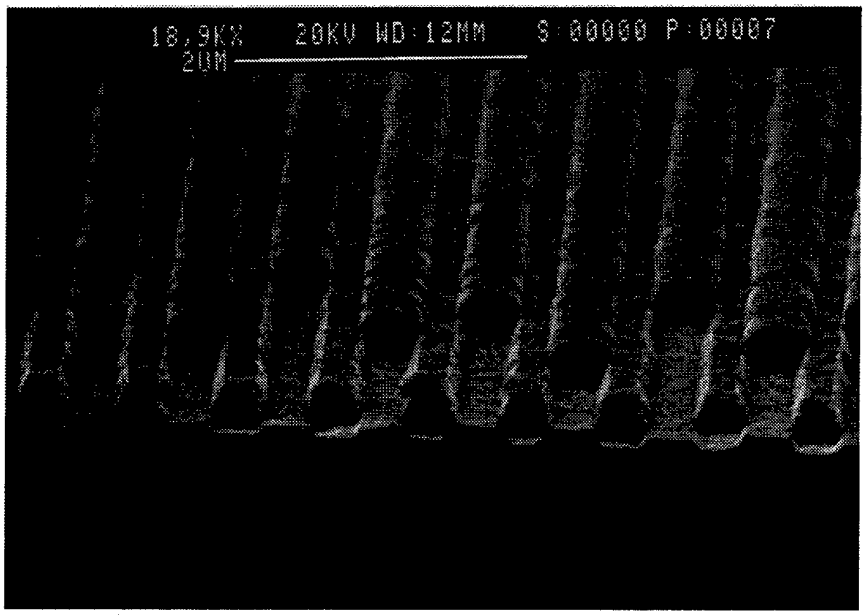

Figure 4.7 - Micrograph suggesting two distinct silicon morphologies

Chapter 5 Conclusion and Recommendations

5.1 Conclusion

This thesis presents the latest step in an ongoing effort to model, fabricate, and characterize optically-resonant periodic electrode structures. In doing so, the work presented here combined the previous achievements in the study of ORPEL structures with the tools necessary to optimize such designs toward potential applications. This work continues the efforts made by other researchers in the pursuit of the next generation of optoelectronic and all-optical devices.

The significant accomplishments made during this research include: the successful use of first-order off-resonance design to initially model our structures, the effective implementation of rigorous coupled-wave analysis into optimization, the demonstrated utility of simplified fabrication methods to construct ORPEL structures, and the production of experimental results that, in several cases, closely match their theoretical predictions. This work has shown that, given a quality waveguide structure to build upon, it is possible to design and construct an optically-resonant structure that satisfies a particular target wavelength. In our case, the thick SOI waveguides provided the most reliable and predictable measurements.

5.2 Recommendations

As mentioned earlier, optical characterization of the $\lambda = 820$ nm structures should be pursued. The inclusion of crystalline silicon's absorption in these models distinguish it from the other two classes of structures. If a comparison of experimental results to theoretical predictions match as well as they did in the other samples, the utility of the modeling and optimization process will be further reinforced.

Both the cross-sectional shape and duty cycle of the grating pose difficulties in linking optimization to fabrication. Not only are more accurate fabrication methods necessary, but for any further optimization, both need to be considered as potential degrees of freedom. Although rectangular profiles and 50% duty-cycles appear to optimize sufficiently, alternative profile shapes and duty-cycles may produce even narrower resonances. For this reason, more work needs to be done to enable these additional degrees of freedom to be incorporated into the optimization process.

The optimization programs produced during the course of this work serve as an effective tool to accurately transform a first-order design into an optimized model ready for fabrication. However, the optimization loops currently written into the programs are only capable of varying the thicknesses of the structure's sub-layers. Additional optimization loops to allow variations to refractive indices should be similarly created.

In addition to further work with a gold gratings, other metals should be explored. Initial modeling and optimization indicate that silver gratings would produce very similar resonance characteristics, but other metals, such as platinum, have yet to be modeled. Platinum silicide (PtSi) is a very important infrared detector material, and the incorporation of PtSi into an ORPEL structure optimized near $\lambda = 1550$ nm could provide a mechanism for silicon-based WDM detectors.

We have not yet commented on the absorption characteristics of ORPEL structures. For the $\lambda = 1550$ nm designs, very little light couples to the transmitted diffracted orders. This is likely due to the fact that the transmission of the diffracted orders through the SiO_2 layer is very low for large angles of incidence. Indeed, it appears that in many of the optimized designs, much of the coupled light is absorbed. That it is absorbed in the metal is clear, since all other materials are lossless at $\lambda = 1550$ nm. At $\lambda = 1064$ nm, silicon has a modest ($10\ cm^{-1}$) absorption which is insufficient to account

for the magnitude of the absorption. Only at $\lambda = 820$ nm does the silicon layer appear to dominate the absorption. It is well-known that coupling from normal incidence will, in general, launch both a right and left traveling wave in the structure. For a structure of infinite width, this results in an infinite standing wave. The standing wave will have intensity peaks either in-phase or out-of-phase with the metal electrode structure. Because of the high absorption in the metal, we speculate that many of the strongest resonances produce a standing wave which is in-phase with the metal. For detection applications, absorption near the metal-semiconductor junction is a favorable property. This is an important area of future investigation.

References

1. NSF Workshop (1994). Optical Science and Engineering: New Directions and Opportunities in Research and Education No. NSF9534. National Science Foundation. Proc. SPIE, **3278**, 286 (1998).

2. L. Canham, "Silicon optoelectronics at the end of the rainbow?" Physics World, (March), 41, (1992)

3. G. V. Treyz, P. G. May, and J. M. Halbout, "Silicon optical modulators at 1.3 μm based on free-carrier absorption," IEEE Letters, **12**, 276 (1991).

4. G. Cocorullo, F. G. Della Corte, R. De Rosa, I. Rendina, A. Rubino, and E. Terzini, "Amorphous silicon waveguides and interferometers for low-cost silicon optoelectronics," Proc. SPIE, **3278**, 286 (1998).

5. S. S. Wang and R. Magnusson, "Theory and application of guided-mode resonant filters", Applied Optics, **32**, 2606 (1993)

6. S. Peng and G. M. Morris, "Experimental investigation of resonant grating filters based on two-dimensional gratings," Proc. SPIE, **2689**, 90 (1996).

7. S. M. Norton, G. M. Morris, and T. Erdogan, "Experimental Investigation of resonant-grating filter lineshapes in comparison with theoretical models," J. Optical Society of America A, **15**, 464 (1998)

8. S. M. Norton, T. Erdogan, and G. M. Morris, "Coupled-mode theory of resonant-grating filters," J. Optical Society of America A, **14**, 629 (1997)

9. N. D. Sankey et. al., "All-optical switching in a nonlinear periodic waveguide structure", Applied Physics Letters, **60**, 1427 (1992)

10. N. D. Sankey et. al., "Optical switching dynamics of the nonlinear Bragg reflector: comparison of theory and experiment,", J. Applied Physics, **73**, 1 (1993)

11. A. E. Bieber, "Coupling and switching in optically resonant periodic electrode structures" Ph.D. Thesis, University of Rochester, 1995.

12. A. E. Bieber et al, "Optical switching in a metal-semiconductor-metal waveguide structure," Applied Physics Letters, **66**, 3401 (1995)

13. A. E. Bieber, "Nonlinear optical interactions in metal-semiconductor-metal waveguide structures," J. Optical Society of America B, **13**, 34 (1996)

14. N. D. Sankey, "Optical switching dynamics of a nonlinear Bragg reflector." Ph.D. Thesis, University of Rochester, 1993.

15. M. G. Moharam and T. K. Gaylord, "Rigorous coupled-wave analysis of planar-grating diffraction." J.O.S.A., **71**, 811 (1981).

16. S. Peng and G. M. Morris, "Efficient implementation of rigorous coupled-wave analysis for surface-relief gratings." J. Optical Society of America A, **12**, 1087 (1995).

17. A. F. Evans, D. G. Hall, and W. P. Maszara, "Propagation loss measurements in silicon-on-insulator optical waveguides formed by bond-and-etchback process." Applied Physics Letters, **59**, 1667 (1991).

18. W. P. Maszara, G. Goetz, A. Caviglia, and J. B. McKitterick, "Bonding of silicon wafers for silicon-on-insulators," J. Applied Physics, **64**, 4943 (1988).

19. E. D. Palik, ed., "*Handbook of Optical Constants of Solids.*" Academic Press, 1985.

20. L. F. Johnson, G. W. Kammlott, and K. A. Ingersoll, "Generation of periodic surface corrugations." Applied Optics, **17**, p. 1165 (1978).

21. "*Properties of Silicon.*" INSPEC, 1988.

The enclosed thesis is unclassified and releasable to the public. (Distribution: A)

ROBERT P. FABRIZZIO II
CPT, AV
United States Army